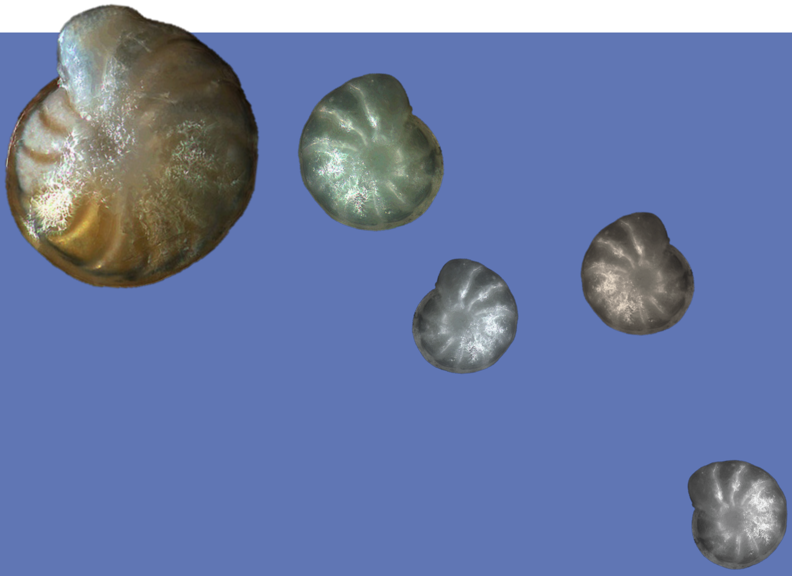

Exploring the MMCO

A high-resolution stable isotope study of ODP site 1264, 17-15.5 Ma.

Cindy Schrader

Supervised by Prof. Dr. Lucas Lourens and Helen Beddow

At the Faculty of Geosciences, Utrecht University, 2014

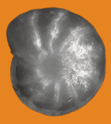

Contents

Abstract

The middle-Miocene Climatic Optimum (MMCO) represents the climax of Neogene warmth and the last large-scale aberration of the global $\delta^{18}O$ record during the Cenozoic transition into the icehouse world. However, it has rarely been studied in high-resolution (<5kyrs). Here, I present new stable isotope data from ODP site 208-1264 (Walvis Ridge, SE Atlantic) placed on an astronomically tuned age model. I further extend the record first published by Liebrand et al (2011) and extended by Mischa Saes (unpublished data, 2013). The data was placed on an astronomically tuned age model covering the interval between 16.97 and 15.46 Ma. This completes a data set covering over 9 million years (~24-15.5Ma) with a high temporal resolution of <5kyrs.

The new stable isotope datasets convey valuable information on the astronomical forcing of the climate throughout the middle Miocene. The first $\delta^{18}O$ drop related to the onset of the MMCO occurs at 17.3 Ma, leading up to a pronounced $\delta^{18}O$ minimum between 17.02 and 16.03 Ma, modulated by the 2.4myr eccentricity cycle. A second striking minimum occurs ~15.6 Ma, modulated by a strong eccentricity maximum. Close inspection of the $\delta^{18}O$ record reveals that the eccentricity is the main pacemaker of climate change during the middle Miocene. The Monterey carbon-isotope excursion is also evident in our data, although we do not capture the entire event. 400kyr filtering reveals the timing of carbon-isotope maximum events (CM1, 2, 3a and 3b) in agreement with records from site 1146 (Holbourn et al, 2007).

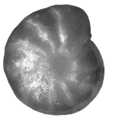

Introduction

Cenozoic climate and the MMCO

The climatic evolution of the Cenozoic Era is characterized by a transition from the greenhouse world during the Cretaceous to the icehouse world in which we live now. The long-term cooling trend commenced in the early Eocene and reached a temperature minimum at the Eocene-Oligocene boundary (fig. 1). Throughout the Oligocene, $\delta^{18}O$ values remained relatively heavy, indicating permanent ice cover on Antarctica with a mass of up to 50% of that of the present day (Liebrand et al., 2011; Lear et al., 2004). Nearing the end of the Oligocene and entering the early Miocene, the Antarctic ice sheets reduced in size and were less stable than during the Oligocene. Nevertheless, a series of positive $\delta^{18}O$ peaks were recognized as short periods of glaciation, also known as "Mi-events" (Miller et al., 1991).

The global cooling trend was also overlain by several short-term warming events that can be identified in the $\delta^{18}O$ record as negative aberrations (Zachos et al., 2001). Currently a lot of research is focused on these warming events, as they can potentially act as analogues for the present-day anthropogenically-induced climate change. The middle-Miocene Climatic Optimum (MMCO) is such an event. Specifically, the MMCO represents the climax of Neogene warmth and is marked as a negative excursion in $\delta^{18}O$ records worldwide ranging between ~17 and ~15 Ma.

A warmer and more humid climate has been reported during the MMCO (Zachos et al., 2001; Mosbrugger et al., 2005) with temperatures increasing 2-4°C globally (You et al., 2009) and up to 6°C at mid-latitudes (Flower and Kennett, 1994). The equator-to-pole latitudinal temperature gradient was weak (Bruch et al., 2007). Also, there were large orbitally paced, volume variations of the East Antarctic Ice Sheet (EAIS). De Boer et al. (2010) claimed that the EAIS decreased up to about 10-25% of its modern volume. In addition, sea level fluctuations of more than 20m have been reported (eg. Flower and Kennett, 1994; Foster et al., 2012; Pekar and DeConto, 2006).

The CO_2 debate and causes of the MMCO

High atmospheric CO_2 values have often been assigned as the main driver of increasing global temperatures in the past. For the MMCO, there has been some debate in the literature as not all the available proxy data seems to agree. Estimates of atmospheric CO_2 concentrations during the MMCO range from well below to more than double the modern level. Pagani et al. (1999) calculated CO_2 levels of 180 to 290ppmv from marine $\delta^{13}C$. Reconstructions by Pearson and Palmer (2000), who used $\delta^{11}B$ to determine marine pH levels, also suggested low CO_2 levels between 140 and 300ppmv. However, more recent publications suggest slightly higher values. Retallack (2009) found concentrations of 850ppmv at 15.6 Ma though CO_2-paleosoil estimations, while Kürschner et al. proposed $p\mathrm{CO_2}$ values of 400-500ppmv based on stomatal frequency data. Foster et al. (2012) reconstructed similar $p\mathrm{CO_2}$ values of 350-400ppmv during the MMCO and 200–260ppmv in adjacent time intervals, also based on boron isotopes.

The contradicting reconstructed CO_2 values make it difficult to determine whether increasing atmospheric CO_2 was the main driver of the MMCO, or that other factors were more important. As most recent papers do find a CO_2 rise compared to the adjacent intervals, a climate system independent of CO_2 is unlikely. It is probable that a combination of several factors led to the initiation of the MMCO.

First, large changes in deep ocean circulation took place leading up to the MMCO. This was due to reconfiguration of interoceanic passages such as the opening of the Central American Seaway and Eastern Tethys Seaway (Holbourn et al., 2007; Bice et al., 2000; Von der Heydt and Dijkstra, 2008).

Second, volcanic activity of the Columbia River Flood Basalts increased between 17 and 15 Ma, which released CO_2 into the atmosphere and amplified chemical erosion. The decrease in eruption rates at 15Ma and the removal of atmospheric carbon dioxide by increased organic carbon burial in Monterey deposits eventually led to cooling and the termination of the MMCO (Hodell and Woodruff, 1994). Third, mountain orogeny ceased during the early and middle Miocene. It was re-established during the late Miocene by the build up of the North American Cordillera (fig. 2), which coincided with the end of the MMCO. Mountain build-up enhances weathering rates that remove atmospheric CO_2, enabling a warmer climate (Foster et al., 2010).

Finally, the timing of the MMCO seems to be connected to astronomical forcing. It was long suspected that large-scale changes in Antarctic ice volume were connected to long-term eccentricity (2.4myrs) and obliquity (1.2myrs) frequencies of insolation (Miller et al., 1991; Wright and Miller, 1992; Beaufort, 1994; Lourens and Hilgen, 1997). This was indeed observed in several high-resolution records. Low seasonality at obliquity nodes in combination with eccentricity minima at 400kyrs and 2.4myrs induced high latitude cooling and ice sheet due to inhibition of summer ice melting (Zachos et al., 2001b; Wade and Pälike, 2004; Pälike et al., 2006a,b; Billups et al., 2002; Abels et al., 2005 Holbourn, 2007; Holbourn, 2014).

ODP leg 208 site 1264

Liebrand et al. (2011) published high-resolution stable isotope records that ranged from the latest Oligocene to the early Miocene (24 to 18.91 Ma) from ODP leg 208, site 1264. Mischa Saes (unpublished data, 2013) extended this record until 16.97 Ma and my goal was to extend the ODP site 1264 record downwards to encompass the MMCO. I extended the record until 15.46 Ma covering an interval of roughly 1.5 million years. I created high-resolution (<5kyrs) $\delta^{18}O$ and $\delta^{13}C$ records from benthic foraminifera (species: *Cibicides mundulus*). Benthic foraminifera are sensitive indicators of environmental change and are extremely useful in reconstructing past ocean systems. Creating these records allowed me to investigate the timing and evolution of the MMCO and how this is connected to orbital forcing.

ODP site 1264 is located on the Walvis Ridge, in the eastern South Atlantic Ocean, just west of South Africa (28°31.95´S 2°50.73´E, fig. 3 and 4). The Walvis Ridge is an ocean ridge ranging from the continental margin of Africa near 20°S latitude to the southwest, connecting to the Mid-Atlantic ridge. The oceanographic conditions of the studied area are uniform and stable, and are assumed to have been similar in the past. The site is located some 400km from the Benguela Current system, which is associated with regions of major upwelling and high productivity (Moore et al., 1984). Due to the geographical distance between site 1264 and the main flow path of the Benguela Current, it is not likely to have a significant influence on site 1264 (fig. 5).

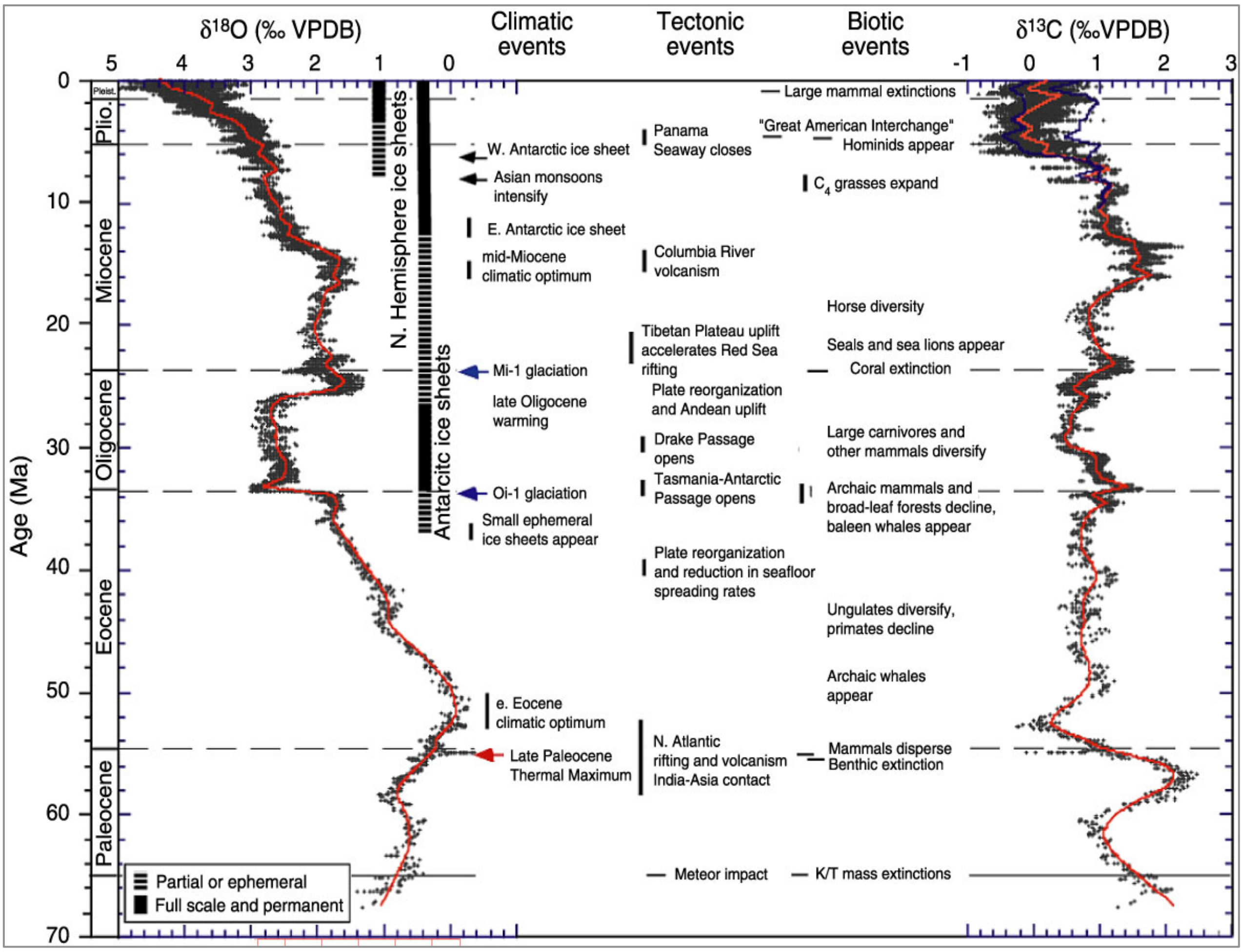

Figure 1. Overview of climate evolution through the Cenozoic. Global deep-sea oxygen and carbon isotope records based on data compiled from more than 40 DSDP and ODP sites (Zachos et al., 2001 and references therein).

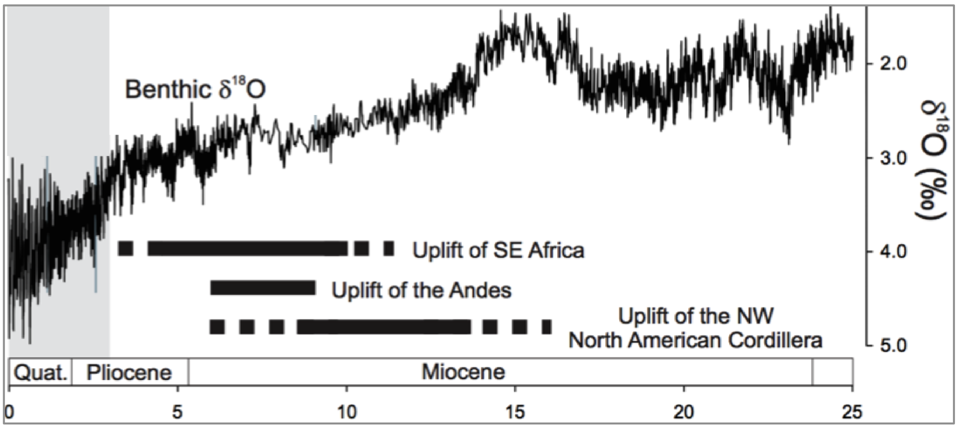

Figure 2. Neogene δ18O record with major geologic uplifting events coincide with the termination of the MMCO. Adapted from Foster et al. (2010) and Zachos et al. (2001).

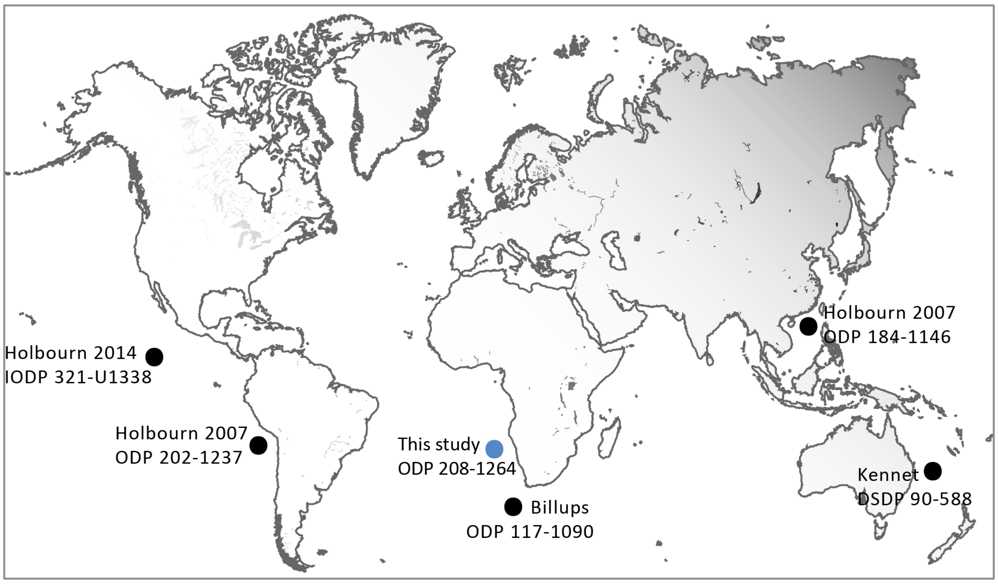

Figure 3. Locations of the coring sites used in this study.

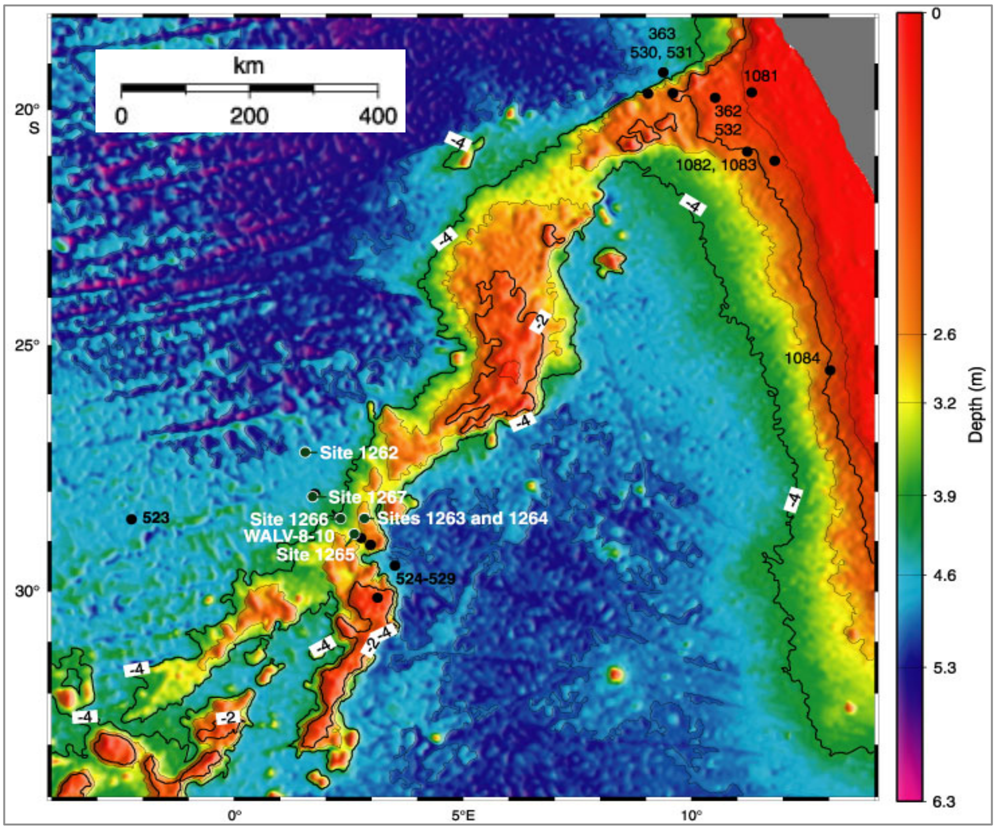

Figure 4. Bathymetric chart of Walvis Ridge, the South African margin, DSDP and ODP sites (black circles), and ODP Leg 208 sites (white circles with green centers). Site 1264 (this study) was the shallowest site in leg 208 (Zachos et al., 2004).

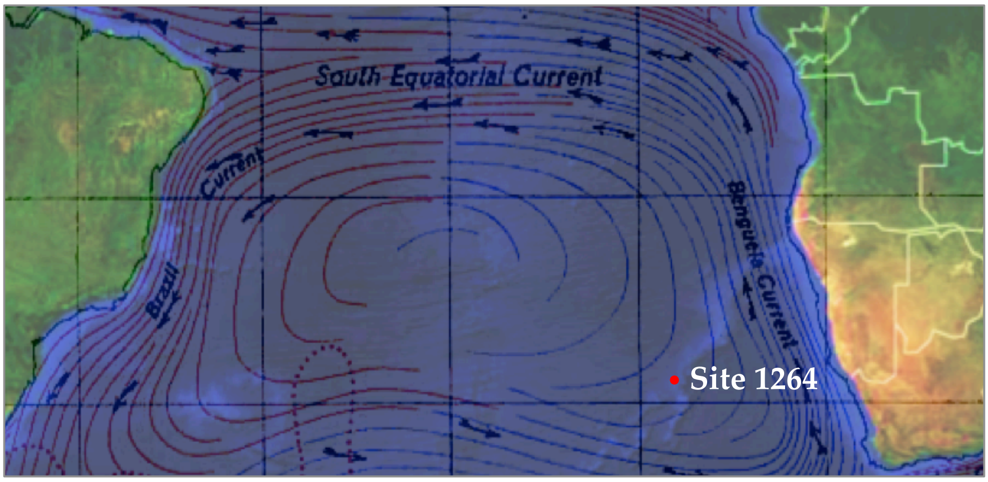

Figure 5. Main currents in the South Atlantic Ocean and the location of ODP site 1264 on the Walvis Ridge.

ODP site 1264 was part of leg 208 and was recovered in the spring of 2003 at a depth of 2505m below sea level. In 1984, the Walvis Ridge was first visited during DSDP Leg 74. Unlike that cruise, ODP Leg 208 was successful in gaining a 100% core recovery due to advances in coring technology and drilling strategies such as multiple-hole composite sections. The Walvis Ridge Transect is a unique location where continuous sedimentary records are present since the Paleogene, including the Paleocene-Eocene thermal maximum (PETM) and the earliest Oligocene Glacial Maximum (EOGM), over a board range of depths. Site 1264 was the end member and also the shallowest site of the Walvis Ridge transect (Zachos, 2004). It is located well above the present lysocline, which lies at a depth of 5 km below sea surface. Below this, the carbonate dissolution rate rapidly increases (Moore et al., 1984). A ~273-m-thick sequence of lower Oligocene to Pleistocene nannofossil ooze was recovered at site 1264.

Up until present, the interval 14-18 Ma has proven to be problematic in most cores. There is a scarcity of continuous sedimentary records for this time period. Most of the sedimentary successions have been affected by carbonate dissolution or have been found to be incomplete as a result in large-scale changes in ocean circulation (Holbourn, 2007). Also the lack of directly correlatable magnetostratigraphic data for integration into orbitally tuned timescales is problematic (Lourens et al., 2004). Although condensed, ODP site 1264 provides a continuous sedimentary record throughout the MMCO (Zachos, 2004). Through correlation with nearby ODP site 1265 (Liebrand et al., 2011) and a rough biostratigraphic age constraint I was able to overcome the lack of magnetostratigraphy for this site.

Proxy records

In this study I used 5 different records derived from the same interval (198.75m–206.65m composite depth, corresponding to ~17-15.5Ma). These records include stable isotope records ($\delta^{18}O$ and $\delta^{13}C$), and three records that function as a proxy for $CaCO_3$ versus terrigenous sediment input, which were used for tuning purposes. These records include: magnetic susceptibility (MS), XRF (in particular: ln[Ca/Fe]), and coarse fraction data.

Stable isotopes are measured as the ratio between the stable light and heavy isotopes of an element. For $\delta^{18}O$ and $\delta^{13}C$ these ratios are $^{18}O/^{16}O$ and $^{13}C/^{12}C$ respectively, calculated relative to the commonly used standard (the Vienna Pee Dee Belemnite, VPDB). Both oxygen and carbon isotopes are recorded in the calcite of foraminiferal tests and are a function of the species-specific variability in element uptake and the composition of the ambient seawater. Natural fractionation processes occur due to mass differences between the isotopes.

For $\delta^{18}O$, fractionation causes the preferential evaporation of light (^{16}O) oxygen relative to heavy oxygen. Therefore, the $\delta^{18}O$ record reflects several environmental parameters. A decrease in $\delta^{18}O$ can reflect a rise in local and/or global seawater temperatures (Epstein et al., 1953), a global seawater $\delta^{18}O$ decrease due to continental ice-sheet decay or a local seawater $\delta^{18}O$ decrease, due to decreasing salinity (Miller et al., 1991; Pierre, 1991 and 1999). Seawater temperature increase and ice-sheet decay are generally linked to minima in insolation.

Fractionation also influences the distribution of carbon isotopes. Similar to oxygen isotopes, there is a preferential uptake of light carbon (^{12}C) relative to heavy ^{13}C during biogenic carbon production. Therefore, an increase in primary productivity causes a corresponding rise in $\delta^{13}C$ values of the surrounding seawater as ^{12}C is locked up in the organic matter. This enables paleo-$\delta^{13}C$ records to be used as proxies for past environmental conditions. These include changes in productivity, terrestrial vegetation and aridity (O'Leary, 1988; Retallack, 2001), and the remineralized nutrient content of a water mass (indicating its age).

The calcite that was used for the stable isotope measurements was acquired from the tests of the benthic foraminiferal species *Cibicides mundulus* (fig. 6). This species has had a common and worldwide occurrence since the Oligocene and prefers a bathyal to abyssal bathymetry (van Morkhoven et al., 1986). Like other foraminifers, *Cibicides mundulus* incorporates elements directly from the ambient seawater into its calcite test. Therefore, the stable isotopes measured from this species record deep-sea conditions. The Shipboard Scientific Party of ODP leg 208 noted a common appearance of *Cibicides mundulus* at site 1264, making it a useful species to base the stable isotopes records on (Zachos et al., 2004).

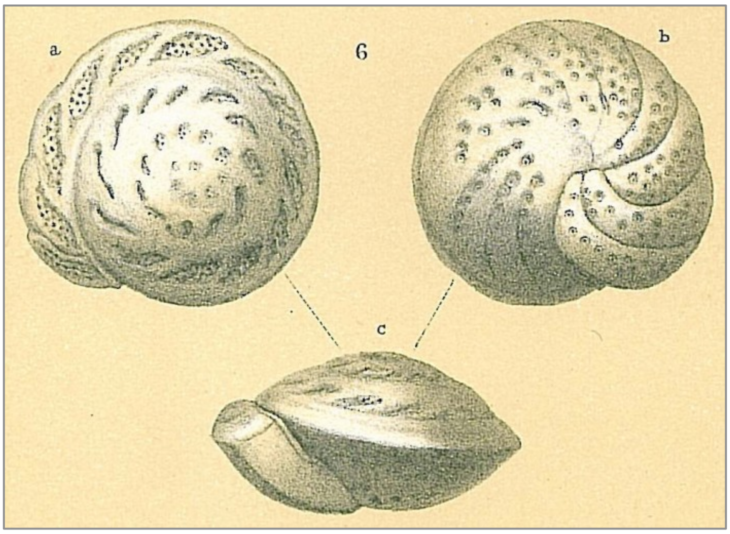

Figure 6. Front, back and side view of foraminifera species *Cibicides mundulus* (Brady, 1884).

Pelagic sediment recovered at site 1264 consists of both biogenic and terrigenous material. The biogenic fraction of the sediment consists of mostly calcium carbonate from calcareous nannofossils and amorphous opal ($SiO_2 \cdot nH_2O$) from diatoms and radiolarians (Robinson, 1990; Rack et al., 1995) and is produced in situ. Terrigenous material consists of fine mud and enters the water column mainly through aeolian dust transport. Down-core variation in the $CaCO_3$ content of the sediment is caused by variability in the influx of terrigenous material relative to the production and dissolution rates of biogenic carbonate. In turn, these factors are connected to climate variability. While the influx of terrigenous material is dependant on the strength of prevailing (monsoonal) winds, $CaCO_3$ production and dissolution is dependant directly on conditions in the water column. I.e., high nutrient availability, low temperatures, high pressure and low pH levels decrease $CaCO_3$ content in the sediment relatively. Therefore, by determining the $CaCO_3$ content of sediment and understanding the climate mechanisms that influence its variability, it is possible to tune the time series data from site 1264 to the astronomical insolation curve, independent from the stable isotope measurements.

I used three proxy records for determining the $CaCO_3$ content of the sediment: magnetic susceptibility, XRF scanning (ln[Ca/Fe]) and coarse fraction data. (1) Magnetic susceptibility measures the degree of magnetization of a sample in response to an applied magnetic field, proportional to a constant. Magnetic susceptibility is generally low for biogenic material, while terrigenous material contains more magnetic minerals (Thompson and Oldfield, 1986). (2) XRF-scanning measures element abundances in the sediment directly. The ratio between calcium [Ca] (biogenic origin) and iron [Fe] (terrestrial origin) is used as a proxy to derive the amount of marine versus terrestrial material in the sediment. (3) The coarse fraction of the sediment (>63μm) is gained as a by-product from sieving as preparation for the stable isotope analysis and contains mostly carbonate foraminifers. The fine fraction (<63μm) however contains mostly nannofossils, juvenile foraminifers and fragments of foraminifera; all bound in a matrix of fine calcareous mud. Because of this, a large coarse fraction points towards a high $CaCO_3$ concentration of the sediment.

Magnetic susceptibility is high when carbonate levels are low (relative to terrigenous material) whereas the ln[Ca/Fe] ratio and the coarse fraction are high when carbonate levels are high as well. Therefore the ln[Ca/Fe] ratio and the coarse fraction tend to correlate well to the inverse of the magnetic susceptibility record. In turn, the $CaCO_3$ records have also been found to correlate well to stable isotope records. Particularly, peaks in carbonate content can be linked to peaks in $\delta^{18}O$ (Steens et al., 1991; Peterson and Prell, 1985, among others) and to insolation minima.

I created a highly detailed astronomically (<5kyr) tuned age model that I based on the magnetic susceptibility record for the largest extent, aided by the XRF ln[Ca/Fe] and coarse fraction data. By doing this I hope to contribute to a more accurate astronomically tuned Miocene Time Scale. Moreover, this research will help generate a better understanding of the relationships between temperature, orbital forcing, ice sheet response and the global carbon cycle during warming events. Investigating the mechanisms operating between its different components increases our understanding of the complex climate system, and helps to constrain and inform modelling studies of climate variability, both for the past and the future.

Methods

Sample preparation and measurement

From the cores of ODP expedition leg 208 site 1264, 400 samples with a down-core width of ~1 cm were taken every other centimeter. The sampled interval, ranging from 198.75 MCD (meters composite depth) to 206.65 MCD, encompasses an interval of about 1.5 million years. This enabled us to create a detailed record with a resolution of <5kyrs per sample, assuming that sedimentation rates were generally constant.

Sample preparation took place at Utrecht University. First the samples were weighed, freeze-dried and weighed again to determine the water content. Subsequently the samples were washed and sieved in 3 fractions: >38μm, >63μm and >150μm. The samples were dried in a 40°C oven and weighed again, in order to calculate the coarse fraction per sample. The >150μm fraction was dry-sieved at 212μm so that juvenile foraminifera were excluded and possible vital effects could not affect the signal. On average I picked 5-15 benthic foraminifera (species *Cibicioides mundulus)* from each sample. From this I selected 2-8 whole and clean specimens to use for the stable isotope measurements, depending on the availability within the sample. Finally the selected foraminifera were submerged in ethanol, crushed and ultrasonically cleansed.

Stable isotope measurements were carried out at the Godwin lab of Cambridge University using a Thermo MAT253 - Gas Bench IRMS. Samples with a weight of <50μg were run on the Thermo MAT253 – Kiel. To calibrate the measurements to the global standard (VPDB), the stable isotope measurements were first compared to the two in-house standards "Carrara Z" and "Atlantis II", both of these were subsequently calibrated to NBS-19 and NBS-18. The precision for the Gasbench is 0.1‰ for both carbon and oxygen. For the Kiel this is 0.06‰ and 0.08‰ respectively.

At Utrecht University, every 20 samples a duplicate sample was measured to investigate inter-laboratory differences. This was done using a Finnigan MAT Kiel III automated preparation system and a Finnigan MAT 253 mass-spectrometer. The samples were calibrated using the in-house standard "Naxos" and the international standard NBS-19. Replicate analyses of samples in the past suggest that analytical precision of this set-up is 0.06‰ for carbon and 0.18‰ for oxygen isotopes. Based on the duplicate samples the average analytical precision for this study is 0.12‰ for both oxygen and carbon measurements.

Finally, on 3 different samples (*201.33, 199.31 and 199.37 MCD*) I carried out ~10 single-specimen runs to investigate variability within samples. These measurements were also carried out at Utrecht University. The values were standardized by subtracting the mean and subsequently plotted together, to compare the distribution to the normal variation (fig. 7). The mean standard deviation of these samples is 0.25‰ for $\delta^{13}C$ and 0.17‰ for $\delta^{18}O$, which represents the error-range for inter-sample variability. These values are slightly higher than the analytical precision, so I chose to use these as error-bar for my stable isotope measurements.

The isotope values were checked for outliers by comparing the sample mass entered into the mass-spectrometer to the total emitted CO_2 as these two have a linear correlation. Also, to correct for the disequilibrium of the ocean water relative to the foraminiferal species I used *(Cibicides mundulus)* I added 0.64‰ to the $\delta^{18}O$ values (Shackleton, 1974).

I combined my new datasets with work previously done for site 1264. This included magnetic susceptibility, XRF-scanning data (ln[Ca/Fe]) and stable isotope records, extending to 263.50 MCD. This work was previously completed at Utrecht University by Rick Seldenrijk (unpublished data, 2013), Mischa Saes (unpublished data, 2013) and Liebrand et al. (2011).

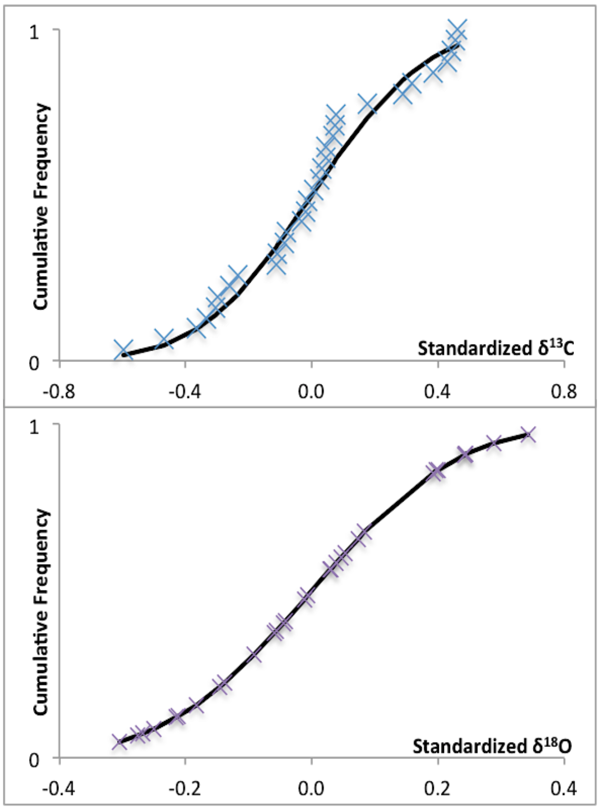

Figure 7. Cumulative frequency distributions for the stable isotope records

Results

Records in the depth domain

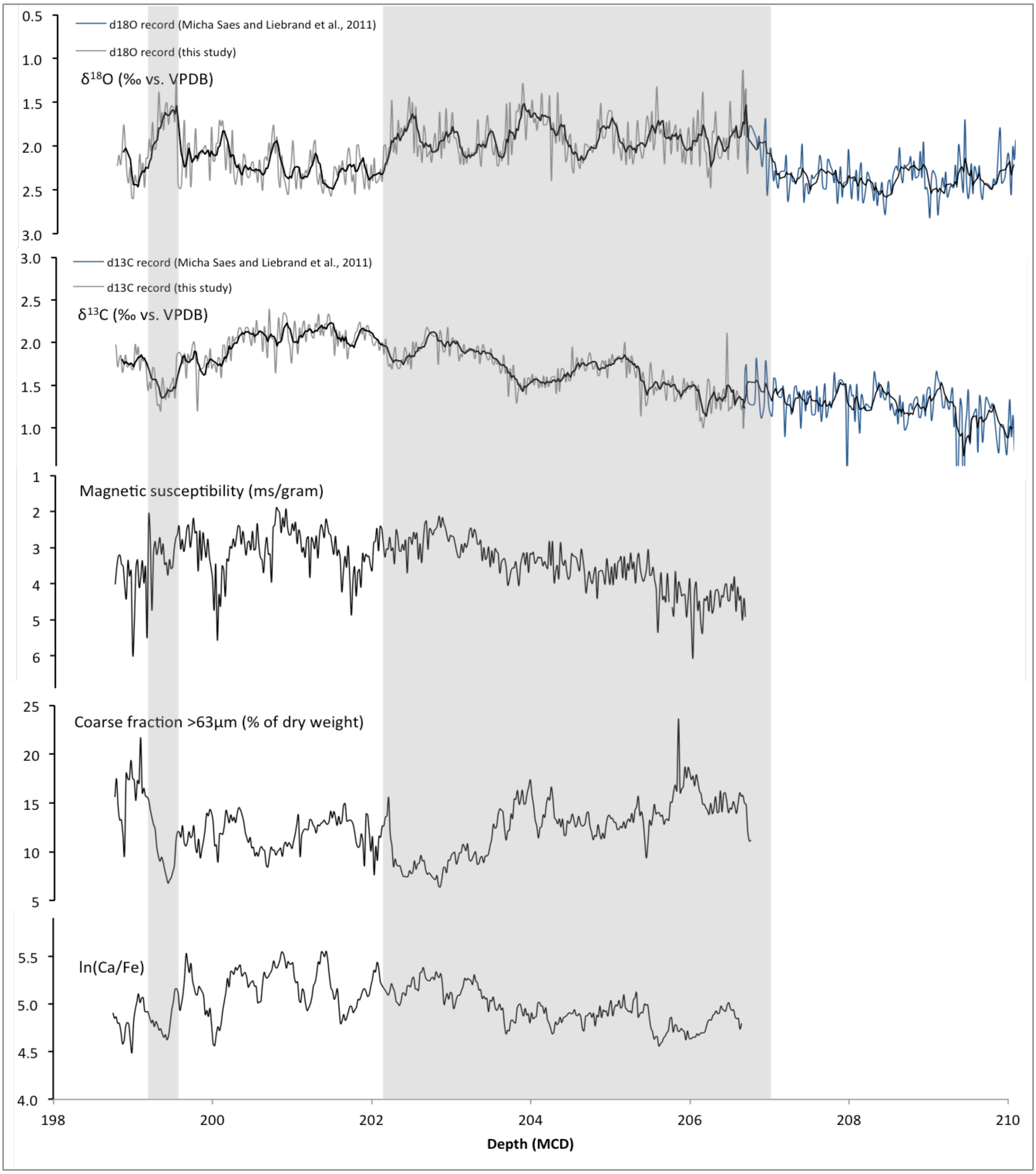

Figure 8. Comparison between the stable isotope records ($\delta^{18}O$ and $\delta^{13}C$), magnetic susceptibility, coarse fraction and ln(Ca/Fe) records for site 1264. The most apparent intervals in the $\delta^{18}O$ record have been highlighted in grey. The $\delta^{18}O$ record is plotted on a reversed y-axis, as is the case consequently throughout this study.

$\delta^{18}O$ values vary from ~1.2‰ to 2.6‰, with an average of 2.0‰. For $\delta^{13}C$, the values range from 1.0‰ to 2.4‰ with an average of 1.8‰. Two intervals are distinguishable in the $\delta^{18}O$ record. Interval A can be recognized at ~199.5 MCD and lasts about 0.5m and interval B can be recognized between ~202.2 and ~207.0 MCD (fig. 8). During these intervals the $\delta^{18}O$ level is clearly reduced to an average of 1.9‰ whereas the average $\delta^{18}O$ outside of the intervals rises to 2.2‰. Interval A coincides with a minimum in $\delta^{13}C$, while in interval B this comparison does not hold. In the $\delta^{13}C$ record maximum values occur between 199.5 and 204 MCD with a short dip at 202.5 MCD (interval C). In general, low $\delta^{18}O$ values seem to correlate well to low $\delta^{13}C$ values. A cross-plot further demonstrates this relationship (R^2=0.33, fig. 9).

To examine cyclicity in the data sets, spectral analysis was preformed using both Wavelet analysis and Blackman-Tukey power spectrums in Analyseries (Paillard et al., 1996). In particular, I investigated in the magnetic susceptibility record, as this record would form the base of my age model (fig. 10). The main frequencies present in the magnetic susceptibility record were found at 48cm and 168cm. The ratio between these two peaks is ~0.28. This closely resembles the ratio between 100kyr and 400kyr components of eccentricity (0.25). These spectral peaks were also recognized in the other data sets, accompanied by a ~1.3m peak in the stable isotope records. Also, in every data set a peak was recognized between 3.0 and 3.3m, although this peak was much lower in amplitude. Visual examination further confirms the link between magnetic susceptibility and $\delta^{18}O$. The cyclicity that is clear in the $\delta^{18}O$ record is also visible with the same duration and phase in the magnetic susceptibility record. This confirms that the magnetic susceptibility record is indeed suitable for tuning.

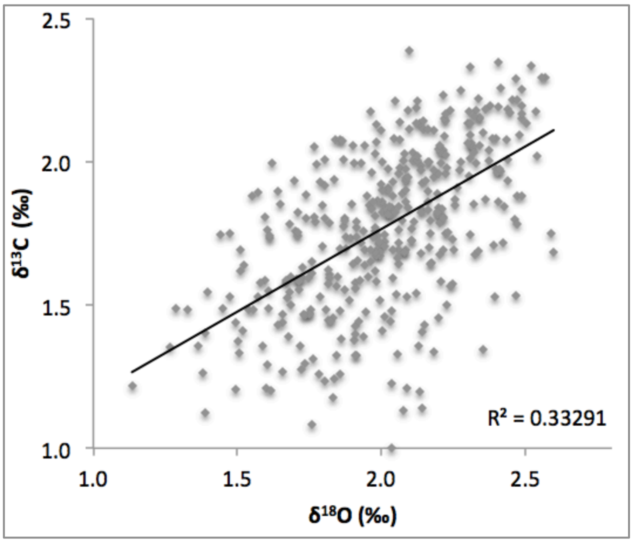

Figure 9. Cross-plot of $\delta^{18}O$ versus $\delta^{13}C$ values. A positive correlation between the two records exists.

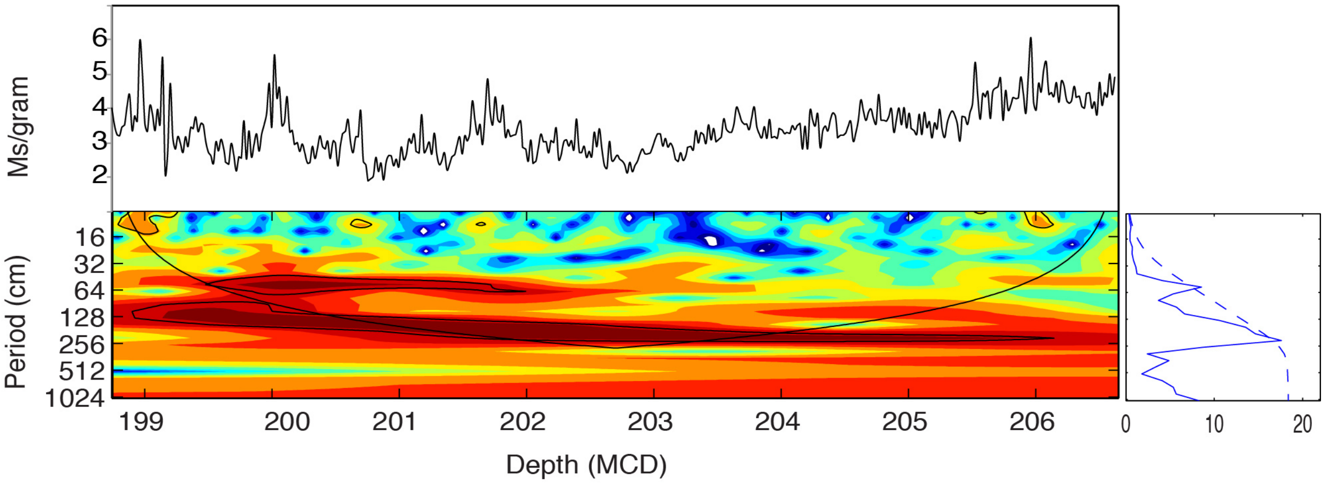

Figure 10. Wavelet analysis for magnetic susceptibility in the depth domain. Main frequencies are found at 48, 106 and 168cm.

Age Model

As a first-order age constraint I expected to use shipboard biostratigraphic and magnetostratigraphic data. However, magnetostratigraphic reversals were absent in my studied interval. Also, the biostratigraphic data that was available seemed to contain large error bars as the calculated sedimentation rates varied from 0 m to almost 30 m/myrs (fig. 12 A). I also investigated the on-ship datum levels (T16, shipboard data, Zachos et al., 2004) that were in fact based on the biostratigraphy, but already took the errors into account. Here, the calculated sedimentation rates seemed more plausible, varying between 5 - 5.5m/myrs.

To ensure the on-ship datum levels were reliable, I followed the approach by Liebrand et al. (2011). They bypassed the magneto-stratigraphic difficulties by correlating site 1264 to the nearby-located ODP site 1265, where the magneto-stratigraphic data was sufficient. They did this by correlating the magnetic susceptibility and colour reflectance (600/450nm) records. Unfortunately, magnetostratigraphic correlation points were also absent at site 1265 in my study interval. Thus, I only transferred the biostratigraphic points from site 1265 to compare the sedimentation rates. Like the on-ship datum levels for site 1264, these were also relatively constant, varying between 5 - 6m/myrs (fig. 12C). This confirmed the reliability of the on-ship datum levels (T16), which I could consequently use to set up the initial age model.

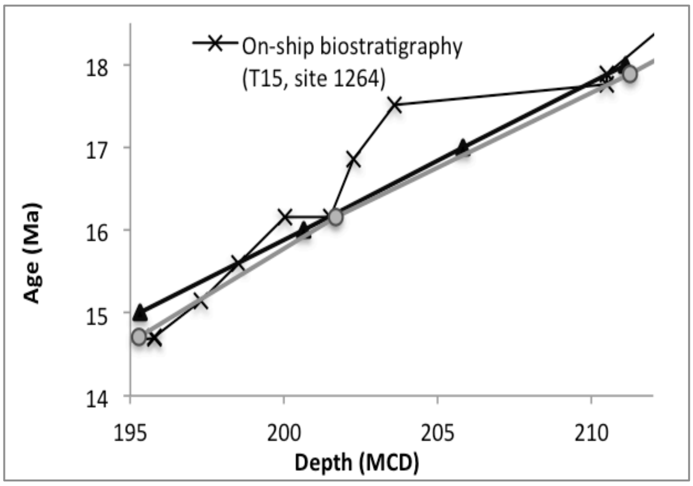

Figure 11. Different potential tie-points for creating a first-order age model.

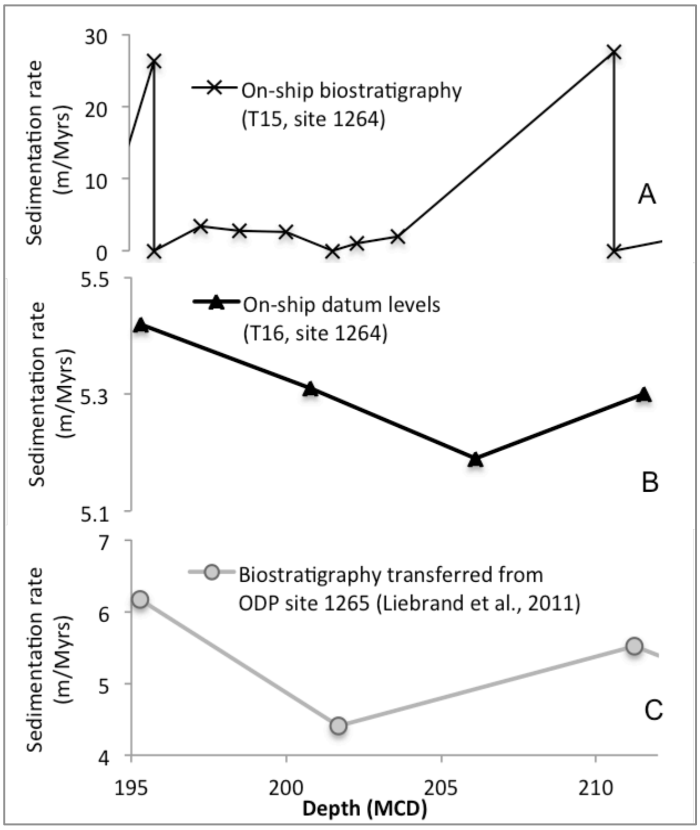

Figure 12. The accompanying sedimentation rates to the potential tie-points. (A) On-ship biostratigraphy (T15, site 1264) shows remarkable sedimentation rate changes, which makes this data questionable.

Spectral analysis

Tuning to the magnetic susceptibility record instead of directly to the stable isotopes enabled me to stay clear of circular reasoning and independently compare changes in the stable isotope records to changes in insolation. I tuned peaks in the magnetic susceptibility record to the 100kyr eccentricity maxima in the astronomical solution (Laskar et al., 2004).

Before commencing with the tuning, I decided to re-perform Wavelet analysis on the magnetic susceptibility record (using the initial age model) to make sure that the cyclicity that I found in the depth domain is indeed Milankovitch variability. For this I standardized the data and removed any linear trends that were present in the data. I applied a notch filter to remove noise and apparent cyclicities of >500kyrs (N=0.002) (fig. 12 and 13).

The main frequencies were found at 333, 111, 40.6, 23.5 and 21.3kyrs. All of these except the 333kyr peak clearly correspond to the main Milankovitch eccentricity, obliquity and even precession cycles. I expect that the 333kyrs peak is either a harmonic of the 111kyr cycle, or related to the 400kyr eccentricity cycle. However, the ratio of 1:3 is not comparable to the 1:4 ratio that is normal for eccentricity. This could either be due to a changing sedimentation rate throughout the record or by the large error-bar of the biostratigraphic tie-points. Since the astronomical relationship with this 333kyr peak is insecure, I tuned the magnetic susceptibility record solely to the 111kyr cycle. Again using AnalySeries (Paillard et al., 1996), I filtered this cycle out of the magnetic susceptibility record (fig. 14).

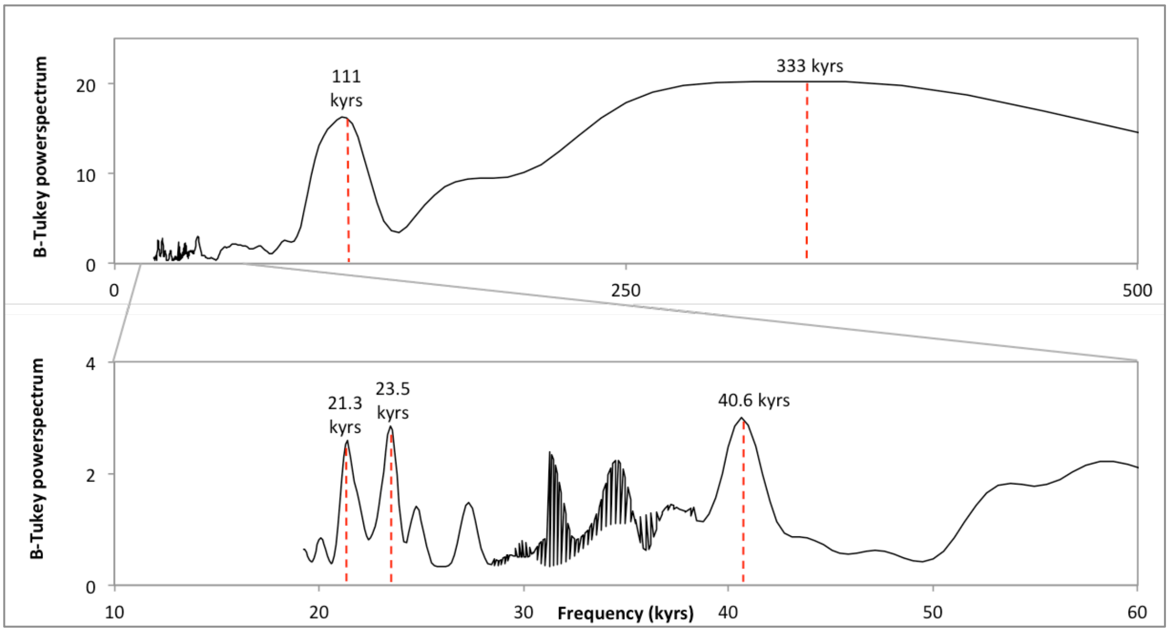

Figure 12. Blackman-Tukey spectral analysis preformed on the magnetic susceptibility record (using the initial age model). Top plot confirms the abundance of the 333 and 111kyr periodicities. The bottom plot is zoomed in to reveal the most dominant high-frequency periodicities (40.6, 23.5 and 21.3kyrs).

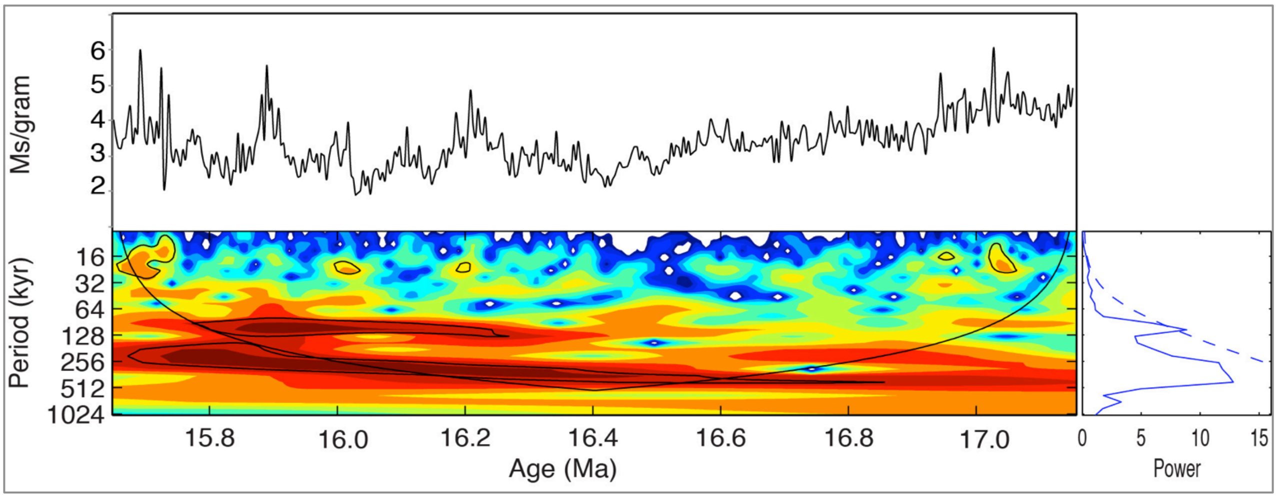

Figure 13. Wavelet analysis for the magnetic susceptibility record (using initial age model). Main frequencies are found at 333 and 111kyrs, with minor peaks at 40.6, 23.5 and 21.3kyrs.

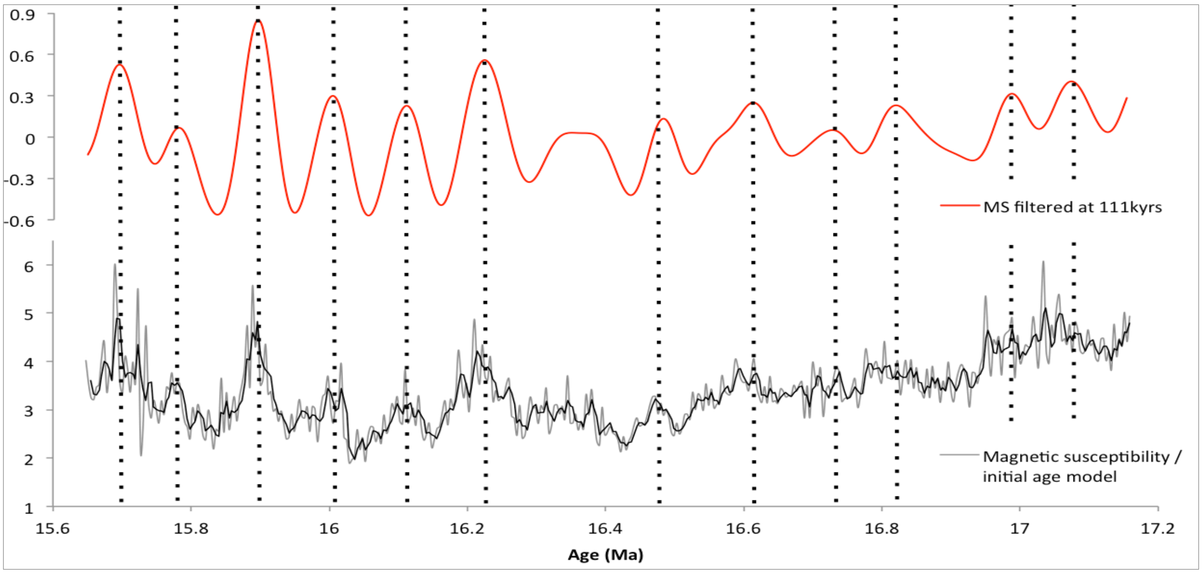

Figure 14. Magnetic susceptibility filtered at 111kyrs. These peaks were tuned to the ~100kyr component of eccentricity.

Assisted by the 111kyr-filtered record and the 5-point average, I tuned the magnetic susceptibility data to the astronomical solution (Laskar et al., 2004). In particular, I used the 100kyr-eccentricity component of insolation for the southern hemisphere summer (21st December) for 28°S (latitude of ODP site 1264). A disadvantage of this method is that any potential lags between eccentricity and the magnetic susceptibility record are discarded. During intervals in the record where the magnetic susceptibility signal was difficult to correlate to the astronomical insolation curve I used the 5-point average of the ln[Ca/Fe] record to assist me.

I linearly interpolated the tuning tie-points and this enabled me to create a detailed astronomically tuned age model for the stable isotope records (fig. 15). To confirm the tuning, I re-preformed Wavelet spectral analysis on the magnetic susceptibility record with the astronomically tuned age model, while keeping all other input factors constant (fig. 16). I also did this for the stable isotope records I generated in this study and on the complete stable isotope record generated for site 1264, including the data from Mischa Saes (unpublished data, 2013) and Liebrand et al. (2011) (fig. 17 and 18).

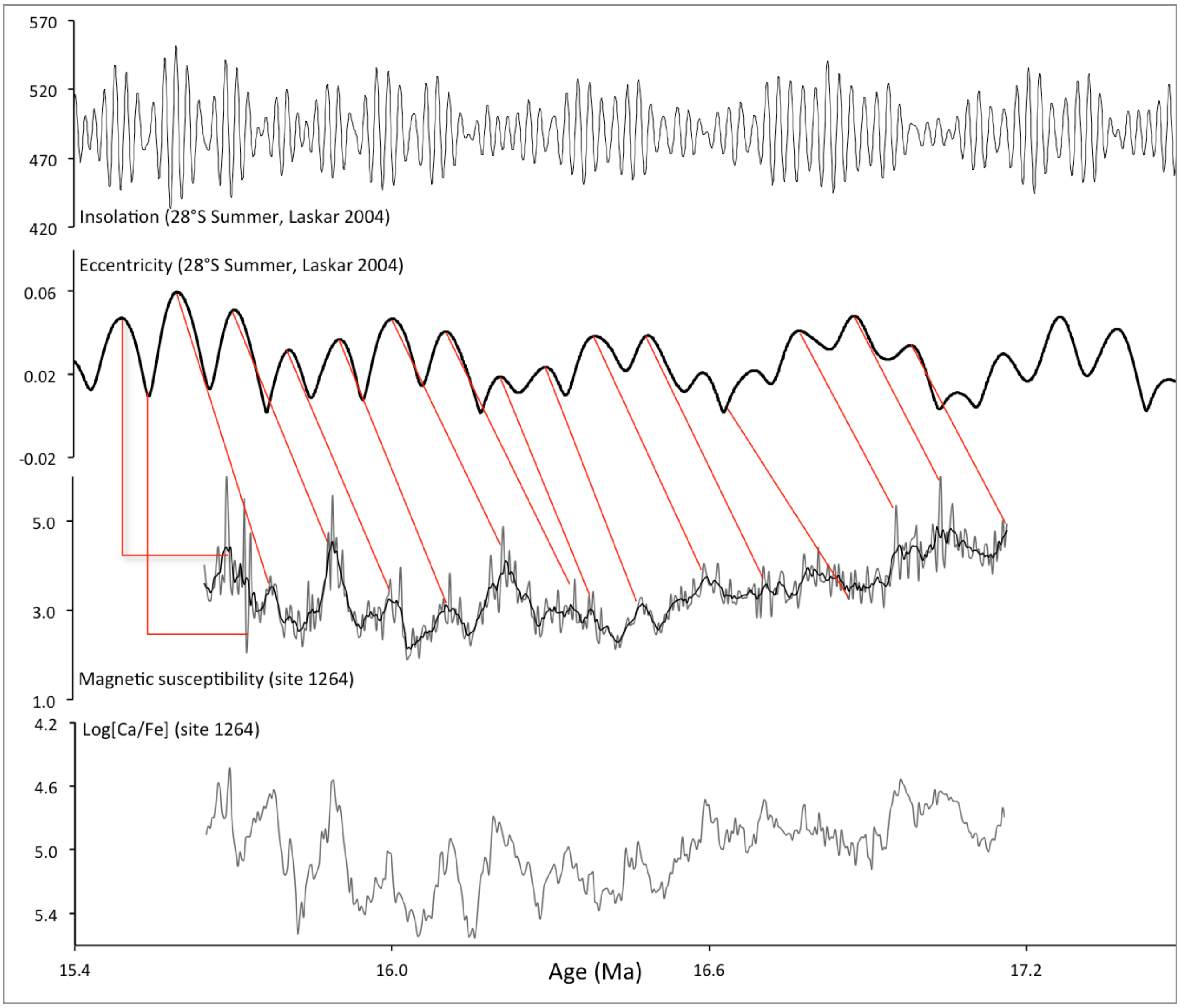

Figure 15. The astronomical insolation curve (Laskar et al., 2004) and the 100kyr component of eccentricity tuned to the magnetic susceptibility record of site 1264. The ln[Ca/Fe] record was used as a reference when the magnetic susceptibility record was not sufficient for tuning.

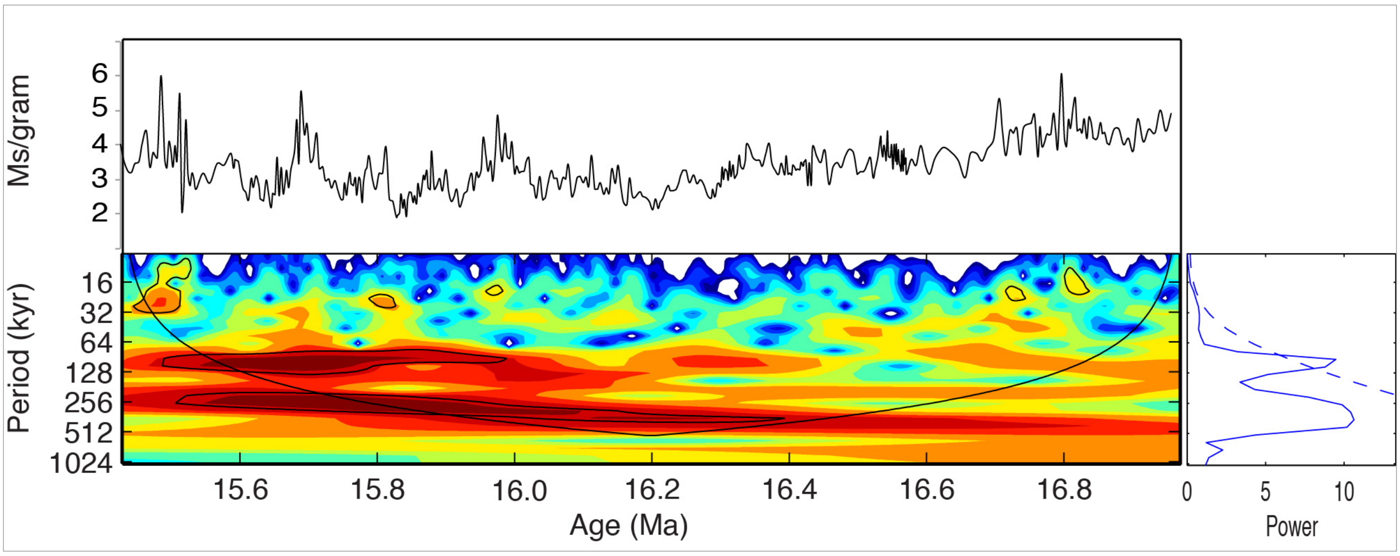

Figure 16. Wavelet analyses of the magnetic susceptibility record using the new astronomical age model. The main frequencies are found at ~100kyrs and ~400kyrs. However, this is simply a consequence of the tuning process.

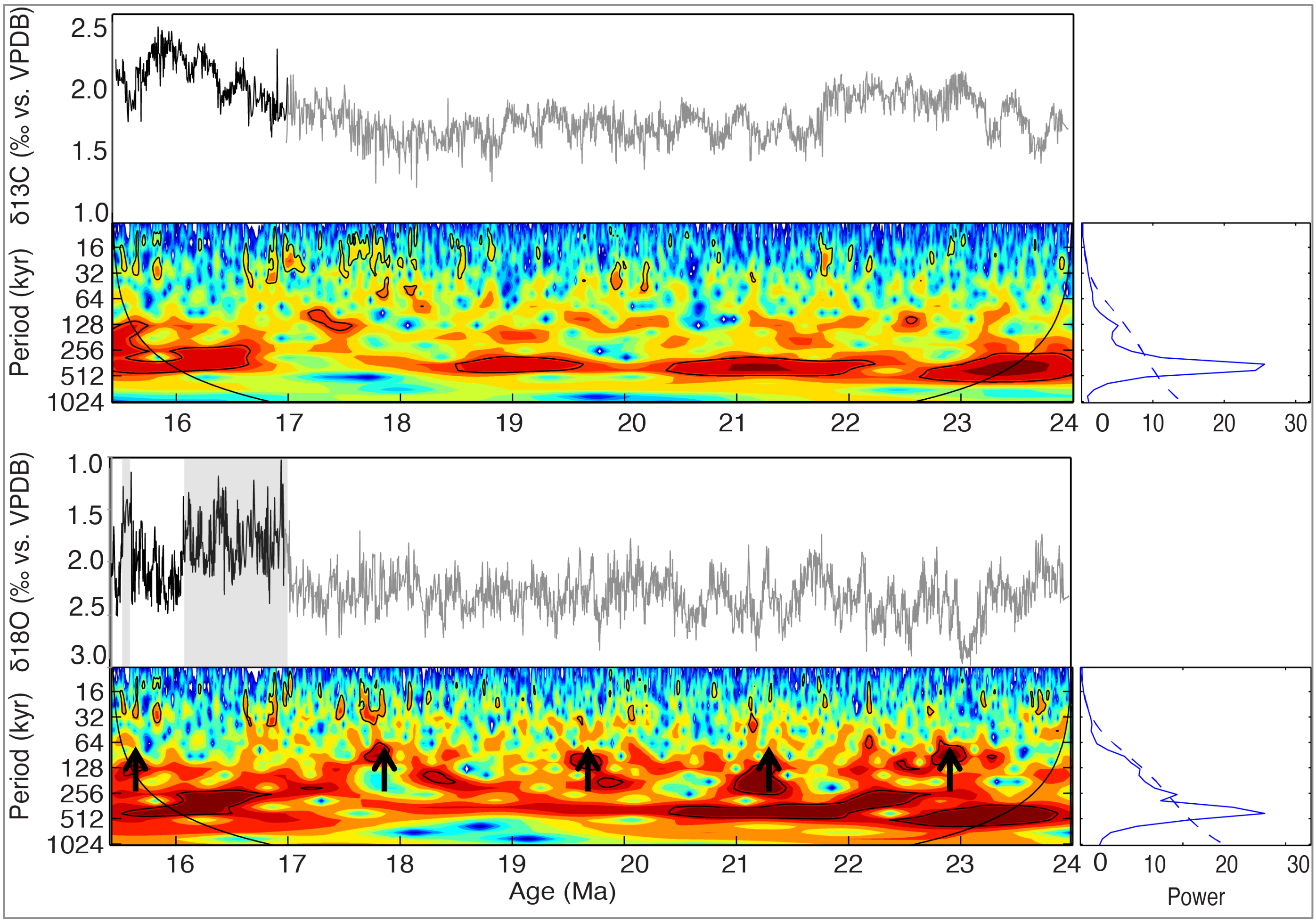

Figure 17. Wavelet analysis of the δ^{13}C and the δ^{18}O records (15.4 – 24 Ma). The main frequency in both records is ~400kyrs. Black arrows represent periods of increased 100kyr cycle dominance.

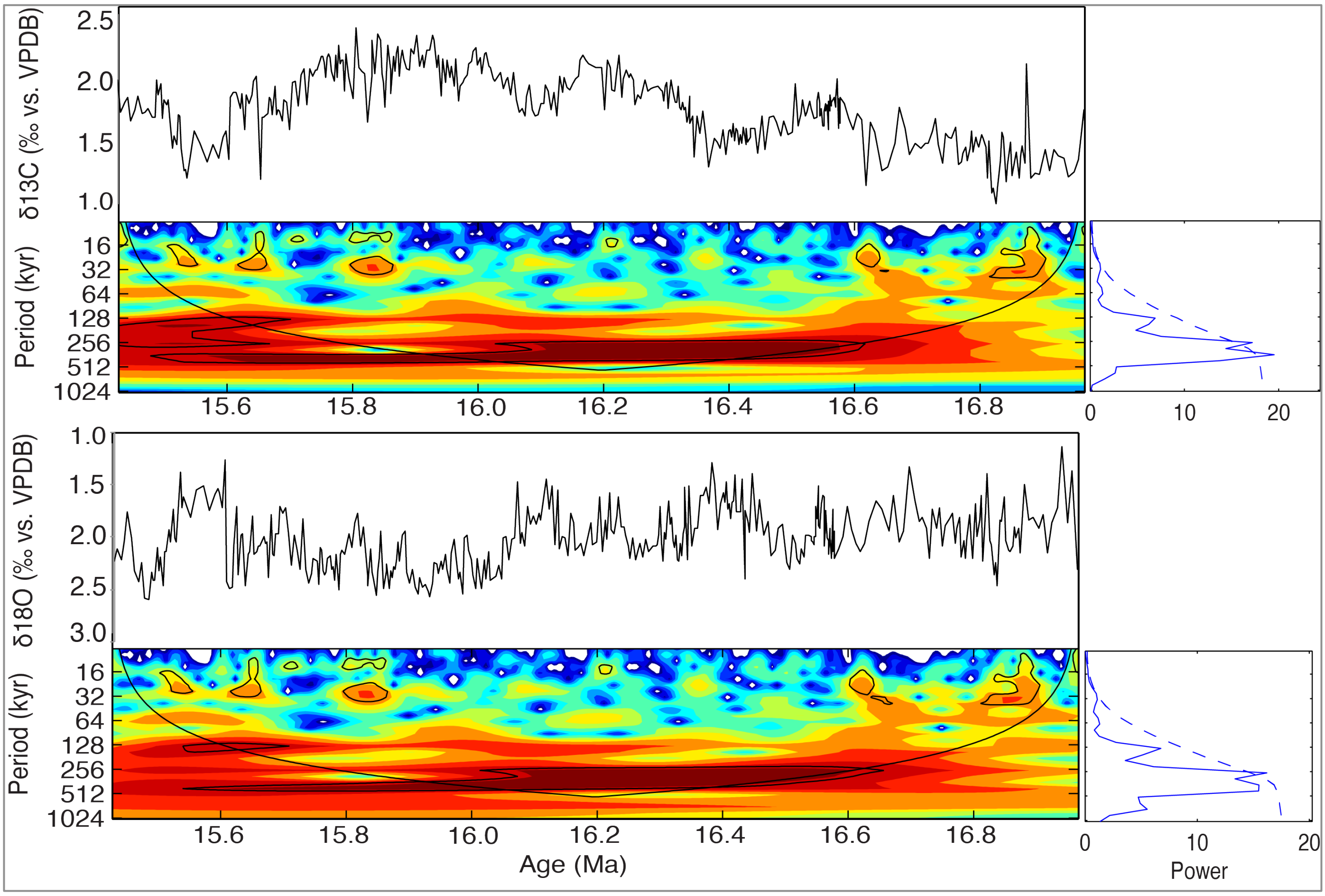

Figure 18. Wavelet analysis of the δ^{13}C and the δ^{18}O records for my study interval (15.4 – 17 Ma).

Stable isotope records

The records created in this study cover the interval from 15.46 Ma to 16.97 Ma. This extends the stable isotope records that were previously measured for this site by Mischa Saes (unpublished data, 2013) (16.97 - 18.91 Ma) and Liebrand et al. (2011) (18.91 - 24 Ma). My data connects well to the pre-existing records for site 1264. Although the age models were created independently, the overlap was <10kyrs.

Over a large part of the studied interval, the $\delta^{13}C$ and $\delta^{18}O$ records are coupled. Peaks in $\delta^{13}C$ correspond to peaks in $\delta^{18}O$ and follow the maxima of the 100 and 400kyr frequencies of eccentricity. During two of the four striking abbreviations in the stable isotope records (interval A-D, fig. 20-22) the $\delta^{13}C$ and $\delta^{18}O$ records were not directly coupled to one-another.

The eldest of these abbreviations in our studied interval is found in the $\delta^{13}C$ data published by Liebrand et al. (2011). This period can be recognized between 23.3 and 21.8 Ma and is marked as 'interval D' in the plots in this paper for easy recognition (fig. 20 and 22). During this interval $\delta^{13}C$ values rise to an average of ~1.5‰, whereas outside of this interval the average is ~1.1‰. This $\delta^{13}C$ rise does not follow the $\delta^{18}O$ record during this period. Except for a brief $\delta^{18}O$ minimum at 23.0 Ma that does coincide with a $\delta^{13}C$ peak, no remarkable decrease occurs in the $\delta^{18}O$ values. The timing of this interval seems to correlate to a maximum in the 2.4myr component of eccentricity (fig. 20).

A second period where the $\delta^{18}O$ and $\delta^{13}C$ records become decoupled is interval B (~202.2 to ~207.0 MCD) and lasts from 17.02 Ma to 16.03 Ma. This interval begins with a $\delta^{18}O$ decrease with values dropping from 2.5‰ to 1.4‰ over a period of ~70kyrs. During interval B $\delta^{18}O$ values vary between 1.3 and 2.3‰. The amplitude variability is the same during the interval as before (when the amplitude varied between 1.8‰ and 2.8‰), while the average value is significantly lower (1.9‰ versus 2.4‰ respectively). The onset of interval B coincides with minima of the 100kyr and 400kyr eccentricity components, while the termination of the event coincides with maxima in the same bands, combined with a 1.2myr-obliquity minimum. The entire interval coincides with a long-term minimum in the 2.4myr eccentricity component. Again, the $\delta^{18}O$ and $\delta^{13}C$ records become decoupled during this interval (fig. 19 and 20). While the $\delta^{18}O$ record shows a pronounced long-term drop, the $\delta^{13}C$ record rises gradually throughout the entire period reaching a maximum after the termination of interval B.

I identified this $\delta^{13}C$ maximum as interval C (fig. 20 and 22). It lasted from 16.4 - 15.6 Ma although a very gradual increase in $\delta^{13}C$ levels already initiated at 17.8 Ma. A rise of almost 1.5‰ took place, from an average of 0.8‰ at 18 Ma to maximum levels of 2.3‰ at 15.8 Ma (fig. 19, 20 and 22). The coupling between the $\delta^{13}C$ and $\delta^{18}O$ records was re-established at 16Ma, at the end of interval B. $\delta^{18}O$ levels rose, coinciding with maximum $\delta^{13}C$ levels. Both stable isotope records were modulated by eccentricity during this interval. Maxima in $\delta^{13}C$ and $\delta^{18}O$ correspond to maxima in in the 400kyr-eccentricity curve. Finally, $\delta^{13}C$ decrease at the end of interval C coincided with a remarkable short-term $\delta^{18}O$ drop: interval A (the '15.6 Ma-event').

Interval A occurs at between 15.6 and 15.5 Ma (~199.5 MCD in the depth-domain). A sharp $\delta^{18}O$

decline at 15.61 Ma characterizes this event with values dropping from 2.5‰ to 1.4‰ in less than 5kyrs. From 15.53 to 15.48 Ma δ^{18}O values rise gradually back to normal (fig. 21A). Interval A coincides with maximum insolation values and a peak in the 100kyr, 400kyr and 2.4myr frequencies of eccentricity and the 1.2myr component of obliquity.

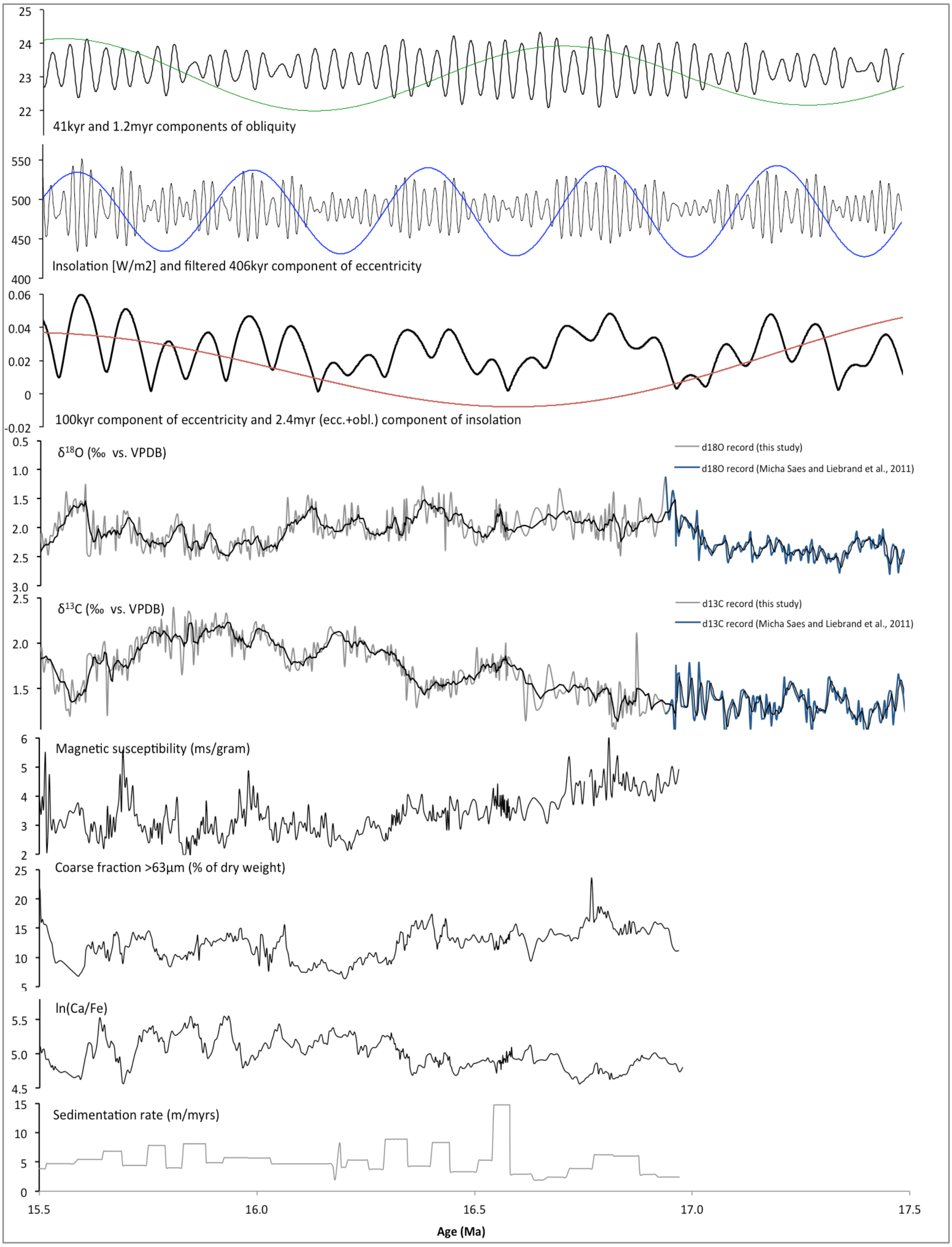

Figure 19. All records used in this study (δ^{18}O, δ^{13}C, magnetic susceptibility, coarse fraction data and the ln(Ca/Fe) record) accompanied by the main astronomical insolation cycles and sedimentation rates. The stable isotope records are slightly extended with data from Mischa Saes (2013, unpublished data) to record the entire MMCO.

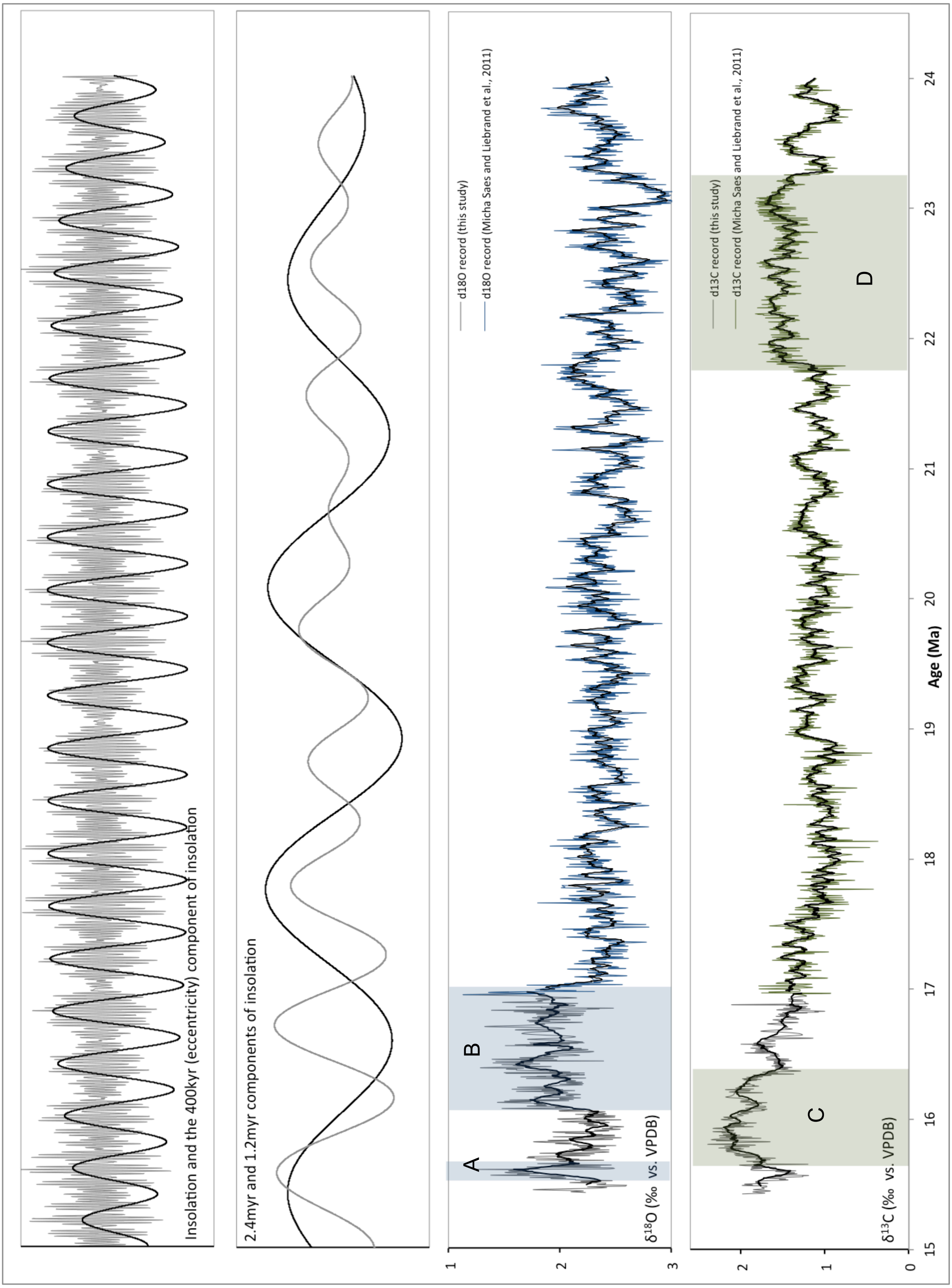

Figure 20. The entire stable isotope data set for site 1264 (~15.5-24Ma) and long-term insolation frequencies.

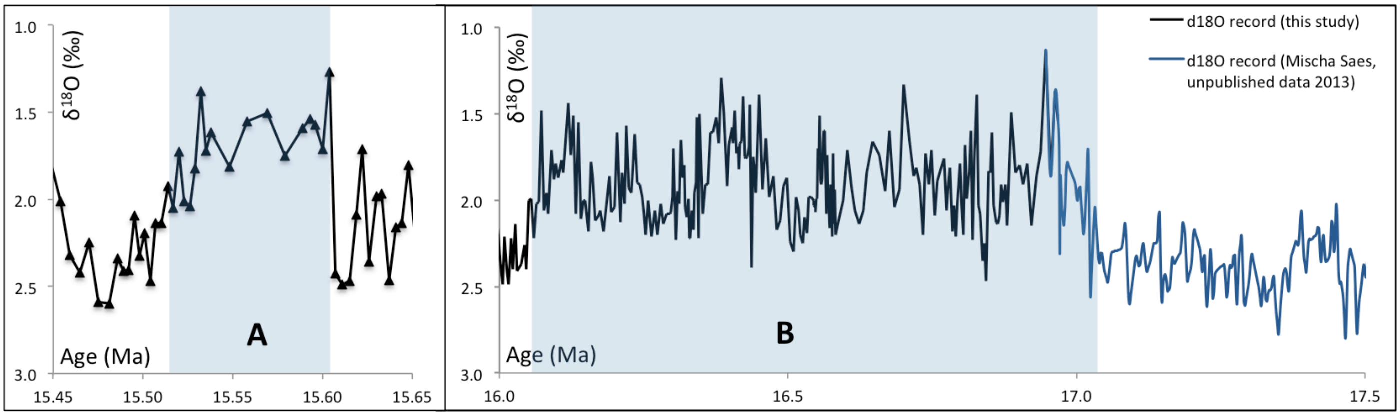

Figure 21. High-resolution graphs of interval A (the '15.6 Ma' event) and interval B (the 'MMCO').

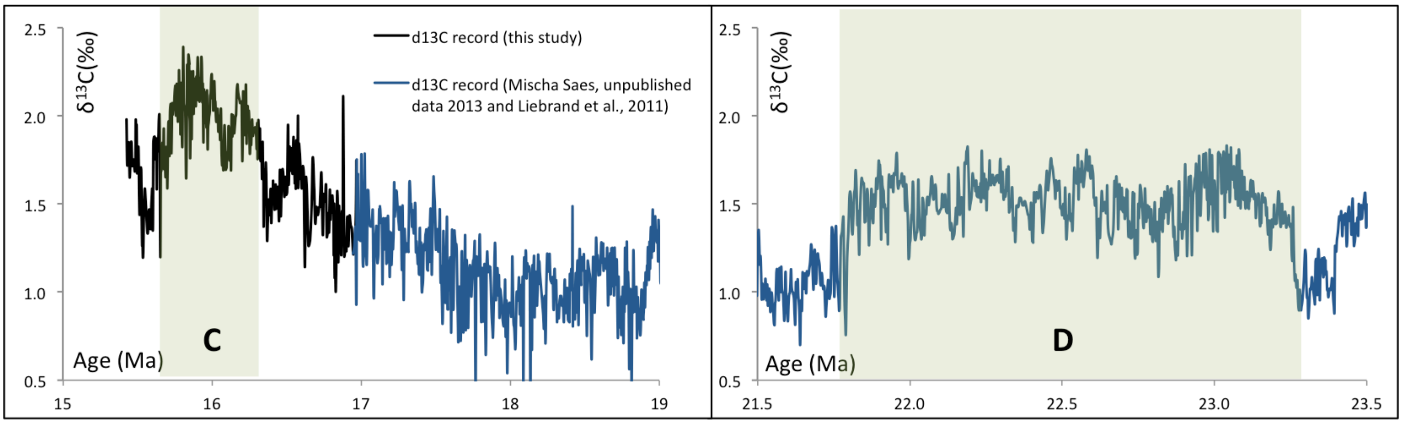

Figure 22. High-resolution graphs of interval C (build-up of the 'Monterey' carbon isotope event) and interval D in the $\delta^{13}C$ record.

Discussion

To further verify my age model and investigate regional differences and gradients between oceanic basins, I compared the records generated in this study to other work that has been done on records from the southern hemisphere for the same time interval (fig. 23-26). Not many high resolution (<5kyr) records have been published covering the entire extent of the MMCO, except for work done by Billups et al. (2002) on a core from site ODP 177-1090 located on the Agulhas Ridge (SE of South Africa) and the stacked record by Zachos et al. (2001). The records by Kennet et al. (1986) and Holbourn et al. (2004) also encompass the entire period, although they are of a less high resolution. This makes it harder to investigate short-term abbreviations in the stable isotope records and the link between climate change and astronomical variability. However, due to lack of more high-resolution records, I did include these records (fig. 23-26) in the comparison. Furthermore, Holbourn et al. (2007 and 2014) also published several records in high resolution, from sites ODP 202-1237, ODP 184-1146 and IODP 321-U1338, all based in the Pacific ocean. However, their studies were based mainly on the Mid-Miocene climatic transition and not on the MMCO itself. Therefore the records do not extend further than 16.8 Ma, just missing the initiation of the MMCO. Due to their high resolution, these records are very useful for comparison with the youngest part of our record encompassing the oldest part of the Monterey carbon-isotope event.

Oxygen isotopes

The MMCO can be recognized as a global event between ~15 and ~17Ma. In this study, the first $\delta^{18}O$ rise leading up to the MMCO initiates at 17.35Ma, whereas the real, long-term warmth interval starts at 17.03Ma (corresponding to the start of 'interval B'). The termination of the climate optimum is not visible in our record, as it only extends to ~15.5 Ma. The stable oxygen isotopes records generated in this study make it clear that temperatures during the MMCO were not constantly high. In the $\delta^{18}O$ record I found two remarkable, distinct abbreviations where temperatures rose significantly $\delta^{18}O$ values dropped ~1‰. These intervals were recognized at ~15.61 Ma, lasting ~100kyrs (interval A), and between 17.02 Ma and 16.03 Ma (interval B).

These intervals are not unique for this site and can be recognized at other sites as well. The '15.6 Ma-event' (interval A) is evident with the same amplitude and duration in the high-resolution records by Holbourn et al. (2007 and 2014) from the ODP 202-1237, ODP 184-1146 and IODP 321-U1338 sites respectively. In the stacked record by Zachos et al. (2001), no '15.6 Ma-event' can be recognized. This is either due to the lower resolution, a less clear expression of insolation in the records or due to an "averaging out" of signals from the different records from which Zachos et al. (2001) created the stacked record. This underlines the importance of the use of high-resolution records when studying the astronomical forcing of the climate system. The long term warm-event during the MMCO (interval B) can be recognised in the records by Billups et al. (2002), Zachos et al. (2001) and Kennet et al. (1986).

The '15.6 Ma-event' corresponds to a maximum in the 100kyr and 400kyr-components of eccentricity and the low-frequency 1.2myr-component of obliquity (fig. 19 and 26). According to Holbourn et al. (2014) the decrease in $\delta^{18}O$ values corresponds to a deep-water warming of ~5 °C, assuming that little ice volume change occurred. Although the $\delta^{18}O$ drop at 15.6 Ma is striking, a closer examination of the record reveals that this event is not unique for this site. In fact, a $\delta^{18}O$ drop can be noticed almost every ~100kyrs, especially between the 15.6-event and the end of interval 'B'. Although the amplitudes of the $\delta^{18}O$ minima differ in magnitude, the timing of the drops corresponds to maxima in the 100kyr cycle of eccentricity (fig. 19). This supports the view of Holbourn et al. (2014), that the 15.6 Ma-event is a striking transient warming event, but merely one of many short-term abbreviations during the MMCO. Furthermore, this supports the role of astronomical-induced insolation as a trigger of intense warming events during the MMCO (Holbourn et al., 2014).

During interval B, $\delta^{18}O$ minima continue to occur every 100kyrs, following the 100kyr eccentricity maxima. However, the $\delta^{18}O$ *maxima* in between the minima are much less pronounced during interval B than after this, making interval B appear to be one long-term warming event. Billups et al. (2002), Zachos et al. (2001) and Kennet et al. (1986) also recognize this long-term $\delta^{18}O$ minimum in their records. At site ODP 177-1090 (Billups et al. 2002) the first $\delta^{18}O$ decline occurs at 17.3 Ma, similar to site 1264, leading up to a pronounced $\delta^{18}O$ minimum between 16.7 and 16.1 Ma. This interval commences ~0.3myrs later than at site 1264 and ends at about the same time. The warm interval is slightly shorter than at site 1264 which could be explained by the higher latitude of site 1090 relative to site 1264. With its position closer to the Antarctic, it experiences more influence of these cold, Antarctic bottom waters. This could possibly have prevented an earlier warming. The stacked record by Zachos et al. (2001) shows a long-term $\delta^{18}O$ minimum between ~17 and 16.2 Ma, although it much less pronounced compared to our record. It is not possible to pinpoint an exact moment when the first warming started, as the decrease is very gradual. The timing of the warm interval is the same, although it lasts ~0.2myrs longer. As the record by Zachos et al. (2001) is composed of a stacking and averaging of 40 different records, attributing this longer duration to a certain location is impossible. The record by Kennet et al. (1986) (site DSDP 90-588) is of a much lower resolution. A minimum is visible between ~18Ma and 15.55Ma, although, unlike the high-resolution records, internal variation within this minimum is not recorded due to a lack of data points.

The occurrence of a long-term 2.4myr eccentricity minimum (fig. 19), which reduces the amplitude of the 400 and 100ky eccentricity cycles, possibly triggered this event. From the computed 100kyr component of insolation (Laskar et al., 2004) (fig. 19) it is evident that the 2.4myr eccentricity minimum especially hinders the eccentricity cycles to develop minima, while the maxima remain intact. The $\delta^{18}O$ record follows this trend. Short-term eccentricity cycles with less pronounced minima possibly disabled the climate system from going back to the "normal, cooler" state in between the eccentricity maxima.

Between 16 and 17 Ma, the climate system was trapped in a full-time warm state but this was not due to insolation alone. Holbourn et al. (2007) linked the occurrence of 400kyr and 2.4myr eccentricity minima together with low seasonality at obliquity nodes, with high latitude cooling and ice sheet expansion in the early Miocene. They also noted that this relationship did not hold during the concurrent obliquity and eccentricity minima at ~16.2 Ma, implying that the middle Miocene climate response was not solely coupled to changes in high-latitude insolation. Additional feedback mechanisms such as tectonic events, circulation patterns or ice-sheet dynamics were required to control the long-term Miocene climate evolution. The decoupling of the $\delta^{13}C$ and $\delta^{18}O$ records during this period further underlines this theory. Something happened that forced the climate system into a full-time warm state while the $\delta^{13}C$ record was not influenced to the same extent.

Carbon Isotopes

In the stable carbon isotope records I recognized 2 abbreviations where the $\delta^{13}C$ levels were significantly elevated, between 23.65 and 21.79 Ma (with a characteristic short-term drop at ~23.3Ma) and between 16.4 and 15.6 Ma (marked as interval 'D' and 'C in fig. 20 and 22 respectively). The first of these two intervals encompasses the Oligocene-Miocene boundary that is defined at 23.03 ± 0.05 Ma. Billups et al. (2002) and Zachos et al. (2001) also recognise this long-term $\delta^{13}C$ maximum. In their records, this interval corresponds exactly in timing and duration and lasts from 23.74 to 21.76 Ma, with the characteristic drop at 23.25 Ma. A benthic foraminifer accumulation rate study by Diester-Haass et al. (2011) attributed the high $\delta^{13}C$ values to an increase in marine primary productivity that was found to be in phase with the long and short term frequencies of eccentricity (Liebrand et al., 2011).

The second positive abbreviation found in our $\delta^{13}C$ record represents the initiation of the "Monterey" positive carbon-isotope excursion ('interval C'). The Monterey excursion was first recognized by Vincent and Berger (1985) and has been recognised worldwide between ~16.9 and ~13.5Ma. However, the deposition of the Monterey Formation already began at 17.8 Ma (Flower and Kennett, 1993). This corresponds to the first $\delta^{13}C$ rise we recognize at our site. Holbourn et al. (2007) recognized nine successive 400kyr cycles during the excursion, which showed a high coherence with the 400kyr eccentricity period. Superimposed on the 400kyr cyclicity they found high frequency (100kyr) oscillations that closely follow the amplitude modulation of the short 100kyr eccentricity period. The nine cycles found by Holbourn et al. (2007) are in contrast to the six carbon-isotope maxima (so called 'CM events') in this interval initially identified by Woodruff and Savin (1991). This difference arose because Holbourn et al. (2007) concluded from their data that carbon-isotope maxima (CM) 3, 4 and 5 consist of two 400kyr cycles, instead of one suggested by Woodruff and Savin (1991) (fig. 26). I filtered the 400kyr frequency out of the three records presented by Holbourn et al. (2007 and 2014) and compared that to the filtered 400kyr frequency of our $\delta^{13}C$ record. The correspondence is striking. This enabled me to identify the oldest 4 carbon-isotope maxima (CM 1, 2, 3a and 3b) mentioned by Holbourn et al. (2007) at our study site as well.

The link between the $\delta^{13}C$ record and the 400kyr eccentricity cycle implies that carbon reservoir changes are modulated by astronomical climate variability. According to Holbourn et al. (2007) insolation maxima favoured the production of carbonate in tropical shallow seas through enhanced monsoons. Insolation minima were characterised by enhanced carbon burial ($\delta^{13}C$ depletion), favouring atmospheric CO_2 drawdown and global cooling. However, Diester-Haass et al. (2013) argue that $\delta^{13}C$ maxima in the middle Miocene are *not* related to changes in marine productivity. During the middle Miocene, $\delta^{13}C$ maxima occur simultaneously with $\delta^{18}O$ maxima. This suggests that periods of cooling and ice build-up were associated with remarkably fast burial of organic carbon and lowered atmospheric CO_2 levels. Diester-Haass et al. (2013) reason that most variability in the carbon isotope record is associated with cyclical sea level variations and induced weathering rates, although this does not explain the full amplitude of the variation. The only exception to this is the last of the CM-events (CM6), which occurs in combination with major Antarctic ice-growth at ~13.5 Ma (outside of our studied interval).

Orbital forcing of the climate system

From the spectral analysis I performed on the stable isotope records (fig. 17 and 18) it is evident that astronomical cycles dominate the variability in the records. Both the $\delta^{18}O$ and $\delta^{13}C$ records are imprinted most clearly with the 400kyr eccentricity signal and to some extent with the 100kyr signal. According to Liebrand et al. (2011), the intervals in the $\delta^{18}O$ record that are strongly dominated by the 100kyr component of eccentricity occur every 800kyrs at site 1264. Spectral analysis of our extended oxygen isotope record (fig 17) confirms this pacing, although it is striking that after ~17Ma (the onset of the MMCO) this pattern seizes to exist. Liebrand et al. (2011) explains the occurrence of the 100kyr-dominated intervals (and related 800kyr pacing) as episodes that coincide with the termination phases of periods of large Antarctic ice sheet expansion. The absence of these 100kyr-dominated intervals between 17.7 and 15.5Ma, coinciding with the long-term warm and non-glacial $\delta^{18}O$ minimum (interval B), confirms this theory. The prominent 100kyr-dominated intervals are not present at all sites. Sites located at a greater depth, and/or are more vulnerable to carbonate dissolution do not show this pattern (Liebrand et al., 2011).

The prominent 100kyr cycles during the MMCO are characterized by their symmetrical shape, sharp decreases and sharp increases. This differs from the well-known saw-tooth shape of the late Pleistocene glacial cycles, implying that different climate dynamics drove these events. According to Holbourn et al. (2014), who also observed this phenomenon in their records, such rapid, high-amplitude $\delta^{18}O$ fluctuations cannot be solely explained by rapid waxing and waning of ice sheets, but must also reflect major changes in deep water temperatures. As these rapid $\delta^{18}O$ fluctuations have been recognized in several different studies (with different water depths and locations) they cannot be attributed to specific water masses, but must instead reflect global climate and circulation changes.

Next to eccentricity, Holbourn et al. (2007) and Zachos et al. (2001) also noticed a significant power in the 41kyr and 1.2myr obliquity cycles in the $\delta^{18}O$ signal. The presence of obliquity cycles suggests that ice-sheets are highly sensitive to obliquity-generated changes in high-latitude insolation, particularly when the polar regions are only partially covered with ice, as was the case during the middle Miocene interval. However, there is no strong obliquity signal in either of the stable isotope records from site 1264 (fig. 17). This could suggest that the influx of Antarctic water is very limited for site 1264, thereby not clearly imprinting the signal. However, it is striking that the sites studied by Holbourn et al. (2007) are situated at lower latitudes and do observe the signal (fig. 3). Why this is the case remains unresolved.

The stable isotope records in this study suggest that eccentricity was the primary pacemaker of the climate change that occurred during the middle Miocene, and that over a large part of the studied interval the $\delta^{13}C$ and $\delta^{18}O$ records were coupled. Peaks in $\delta^{13}C$ correspond to peaks in $\delta^{18}O$ and follow the maxima of the 100 and 400kyr frequencies of eccentricity. The seasonal insolation cycle can drive changes in biosphere productivity over long (eccentricity) time scales, due to the long residence time of carbon in the ocean (Pälike et al., 2006b; Liebrand et al., 2011). High $\delta^{13}C$ values indicate periods of increased carbon burial, which declines atmospheric pCO_2 concentrations. In turn, this favours global cooling and ice-sheet expansion resulting in high $\delta^{18}O$ levels.

Insolation-forced changes in the carbon cycle most likely modulated the climate over large part of the Oligocene and Miocene at site 1264, as was also found by Pälike et al. (2006b) and Liebrand et al. (2011). However, during periods where the $\delta^{13}C$ and $\delta^{18}O$ records were de-coupled other mechanisms acted upon the climate system. The $\delta^{13}C$ rise associated to the Oligocene-Miocene boundary ('interval D') indicates an increase in marine primary productivity that did *not* cause global temperatures to rise. Likewise, the long-term $\delta^{18}O$ minimum related to the warmest episode of the MMCO ('interval B') was not directly linked to a $\delta^{13}C$ minimum. Instead, throughout this interval $\delta^{13}C$ values increased gradually, reaching a maximum at ~16 Ma. The termination of interval B coincides with the last strong $\delta^{13}C$ rise before reaching its maximum. As noted before, high $\delta^{13}C$ levels are related to atmospheric CO_2 depletion. Most likely, CO_2 levels at the end of interval B became so low that a threshold was crossed, forcing the climate system back into a temporary cold state.

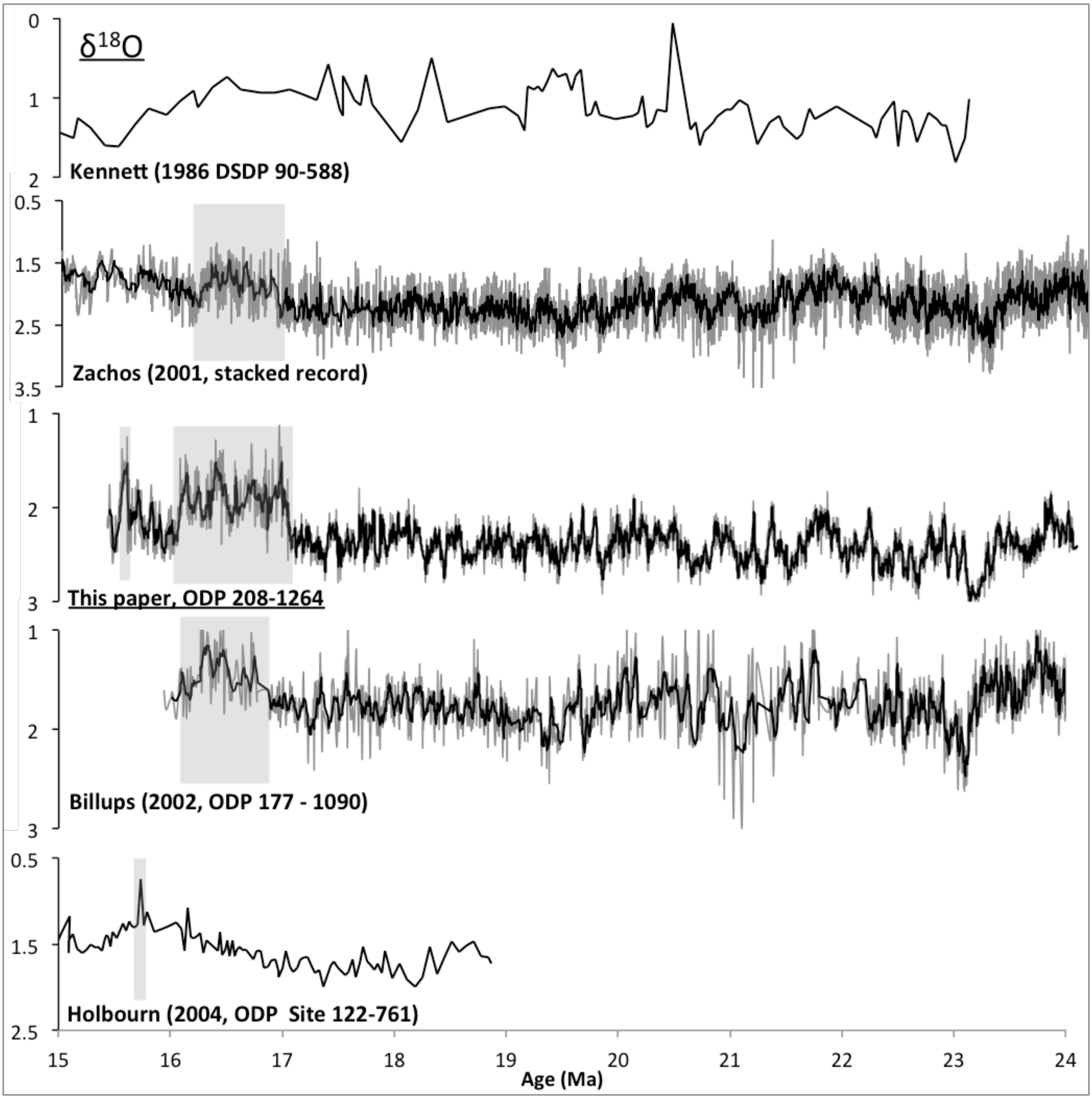

Figure 23. The full δ18O record for site 1264 (15-24Ma), compared to the δ18O records by Kennett et al. (1986), Zachos et al. (2001), Billups et al. (2002) and Holbourn et al. (2004). Black lines in the high-resolution graphs represent the 5-point averages. Grey shading marks interval A and B, the '15.6Ma-event' and the initiation of the MMCO respectively.

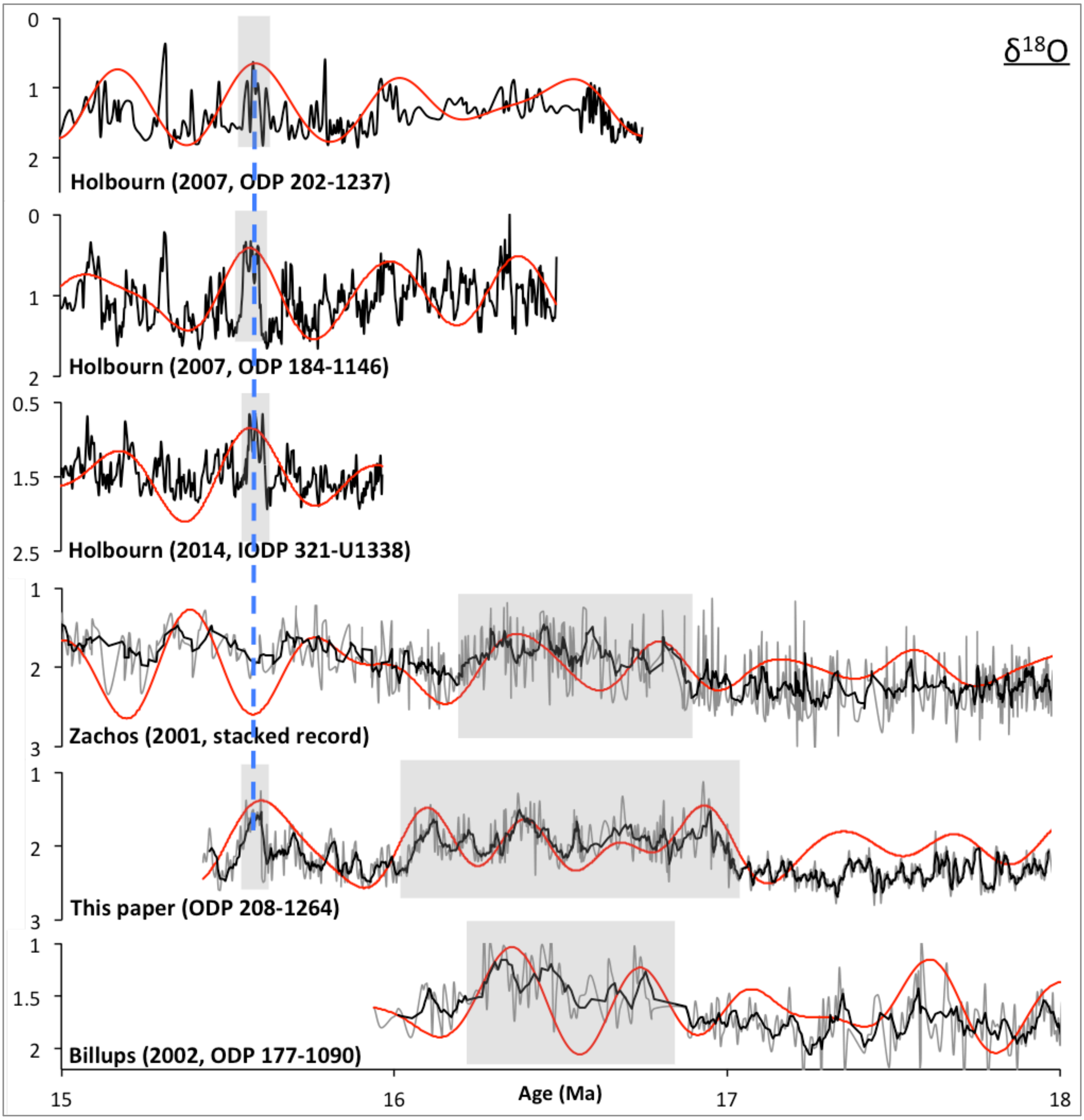

Figure 24. The δ18O record for site 1264 in higher detail (15-18Ma), compared to the δ18O records by Holbourn et al. (2007 and 2014), Zachos et al. (2001) and Billups et al. (2002). Grey intervals mark interval A and B, the '15.6Ma-event' and the 'MMCO' respectively. Red graphs are the 400kyr filters of the corresponding δ18O records. A clear correlation exists between our site (1264) and records by Holbourn et al. (2007 and 2014) for interval A. However, no clear correlation exists between the records during the MMCO.

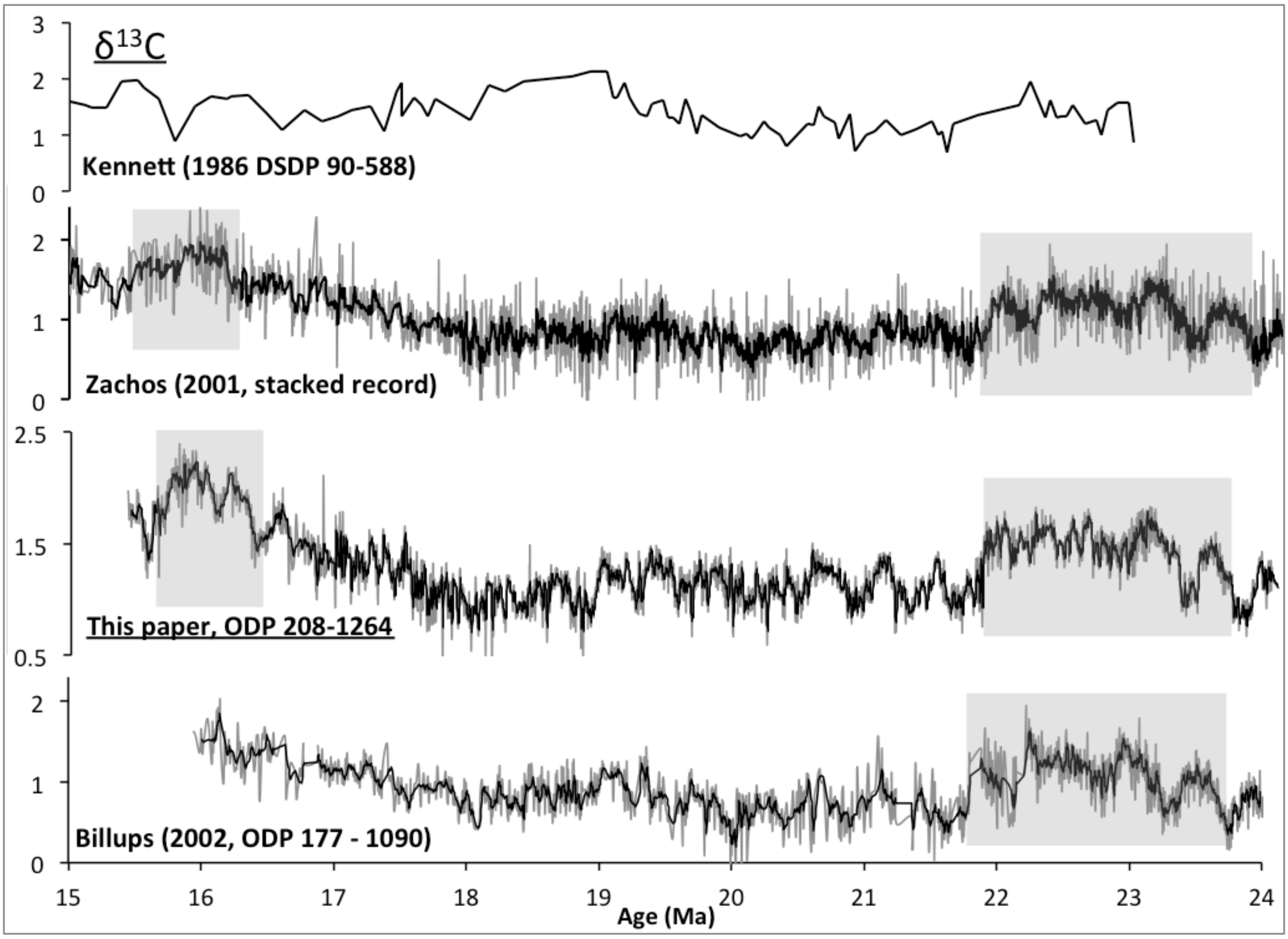

Figure 25. The full δ¹³C record for site 1264 (15-24Ma), compared to the δ¹³C records by Kennett et al. (1986), Zachos et al. (2001), and Billups et al. (2002). Grey shading marks interval C (the initiation of the Monterey carbon-isotope excursion) and D (elevated δ¹³C following the Oliogocene/Miocene boundary).

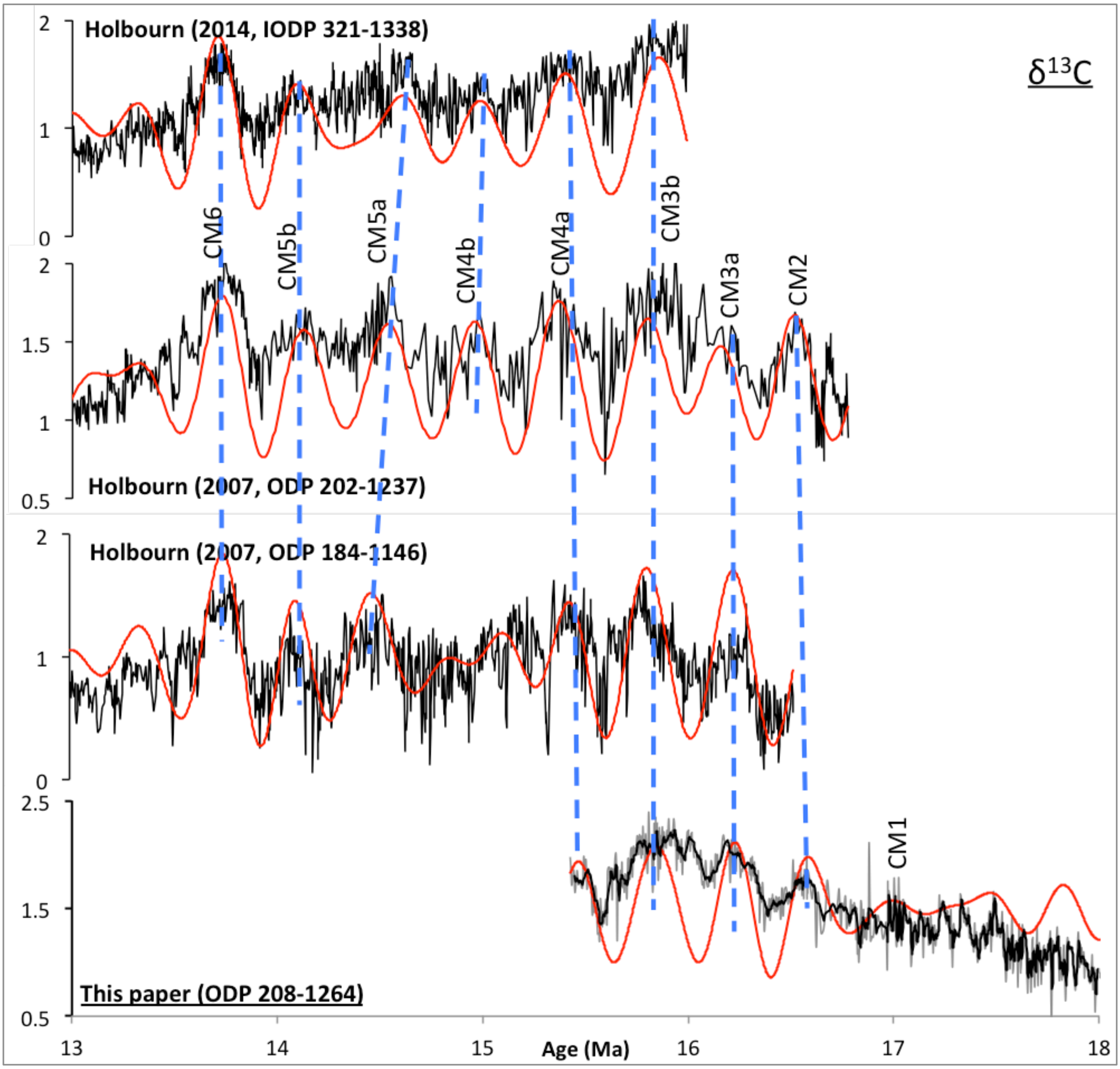

Figure 26. Comparison of the δ13C record of site 1264 to the high-resolution records by Holbourn et al. (2007 and 2014). Red graphs correspond to the 400kyr filters of the different records. Blue dashed lines convey their correspondence to one another. Carbon-isotope maxima (CM) as described by Holbourn et al. (2007).

Conclusions

Orbitally tuned stable isotope records from ODP site 1264, located on the Walvis ridge in the SE Atlantic, provide new insights into the effect of astronomical insolation variability on the evolution of the climate throughout the middle Miocene. The interval between 18 and 14 Ma has been proven to be problematic due to a scarcity of continuous sedimentary records. However, this study extended the records first published by Liebrand et al. (2011) to ~15.5 Ma, encompassing the MMCO and the beginning of the "Monterey" carbon-isotope excursion.

The first $\delta^{18}O$ drop related to the onset of the MMCO occurs at 17.3Ma, leading up to a pronounced minimum between 17.02 and 16.03 Ma. The timing of this event occurs ~0.3myrs earlier at site 1264 than at ODP site 177-1090 (Billups et al. 2002), possibly explained by the higher latitude of site 1090 relative to site 1264 or due to age model differences. The long-term warm event during the MMCO corresponds to a 2.4myr eccentricity minimum. This decreased the amplitude of the 100 and 400kyr eccentricity maxima, which trapped the climate in a ~1myr 'greenhouse' state.

A second striking $\delta^{18}O$ minimum is found at ~15.6 Ma, coinciding with a minimum found in the records by Holbourn et al. (2007 and 2014) and a strong eccentricity maximum. The 15.6 Ma-event is a striking transient warming event, but merely one of many short-term abbreviations during the MMCO related to the occurrence of 100kyr eccentricity maxima. This supports the role of astronomical-induced insolation as a trigger of intense warming events during the MMCO. In particular, we find that eccentricity was the primary pacemaker.

The carbon isotope record records two significant long-term maxima. Between 23.65 and 21.79 Ma enhanced productivity caused an elevation of the $\delta^{13}C$ record related to the O/M boundary. At 17.8 Ma $\delta^{13}C$ values gradually increased again, related to the onset of the Monterey carbon-isotope event at ~16.9. Holbourn et al. (2007) recognized nine successive 400kyr cycles during the excursion, which showed a high coherence with the 400kyr eccentricity period. Through comparison of the 400kyr filtered records we recognised the eldest four carbon-isotope maximum events (CM1, 2, 3a and 3b). Unlike the $\delta^{13}C$ increase at the O/M boundary, the Monterey-event was not related to productivity (Diester-Haass et al., 2013). Instead, cyclical sea level variations and induced weathering rates were large contributing factors.

During the middle Miocene there was a strong coupling between the climate system and changes in the oceanic carbon reservoir. Peaks in $\delta^{13}C$ correspond to peaks in $\delta^{18}O$ and follow the maxima of the 100 and 400kyr frequencies of eccentricity Periods of elevated $\delta^{18}O$ levels (corresponding to cold phases and possible glaciation) were coupled to periods of high $\delta^{13}C$ values (corresponding to periods of increased carbon burial and an associated drawdown in pCO_2 concentrations) and vise versa. In turn, maxima in the stable isotope records were related to maxima in the 100 and 400kyr bands of eccentricity. Thus, insolation-forced changes in the carbon cycle most likely modulated the climate over large part of the Oligocene and Miocene at site 1264.

We find that during two intervals the $\delta^{13}C$ and $\delta^{18}O$ records were de-coupled other mechanisms acted upon the climate system. During the $\delta^{13}C$ rise associated to the Oligocene-Miocene boundary ('interval D') enhanced productivity that did not cause global temperatures to rise. Similarly, the long-term warm phase of the MMCO ('interval B') the was not directly linked to a $\delta^{13}C$ minimum. Instead, throughout this interval $\delta^{13}C$ values increased gradually, reaching a maximum at ~16 Ma. Most likely, CO_2 levels at the end of interval B became so low that the climate system was forced back to a temporary cold state.

Acknowledgements

I would like to thank Prof. dr. Lucas Lourens for giving me the opportunity to take part in this research, for his supervision, data discussion and review. Furthermore my gratitude goes out to Helen Beddow who supervised me on day-to-day basis. She was always ready to answer my many questions and provided me with a lot of valuable input and critical reviews of my thesis. My thanks also go out to Dominika Kasjaniuk for washing a great deal of my samples and her practical help in the Strat-Pal lab. Additionally, my thanks go out to dr. Diederik Liebrand for aiding me with his data and comments and to the Ocean Drilling Program and Bremen University for providing the cores and assistance during the sampling procedure. I also am in debt of the staff of the Godwin Lab at Cambridge University. Prof. dr. David Hodell, Jenny Roberts; thanks for helping me find my way around Cambridge and the lab and thank you James Rolfe for running all (400) samples on the mass spectrometer for me.

References

Abels, H.A., Hilgen, F.J., Krijgsman, W., Kruk, R.W., Raffi, I., Turco, E., Zachariasse, W.J. (2005) Long-period orbital control on middle Miocene global cooling: integrated stratigraphy and astronomical tuning of the Blue Clay Formation on Malta. Paleoceanography 20.

Beaufort, L. (1994) Climatic importance of the modulation of the 100 kyr cycle inferred from 16 myr long Miocene records, Paleoceanography, 9, 821–834.

Berger, W.H., Bonneau, M.-C., and Parker, F.L., (1982) Foraminifera on the deep-sea floor: lysocline and dissolution rate. Oceanol. Acta, 5(2):249–258.

Bice, K. L., Scotese, C. R., Seidov, D., and Barron, E. J. (2000) Quantifying the role of geographic changes in Cenozoic ocean heat transport using uncoupled atmosphere and ocean models, Earth Planet. Sci. Lett., 161, 295–310, 491, 509

Billups, K., Channell, J. E. T., & Zachos, J. (2002). Late Oligocene to early Miocene geochronology and paleoceanography from the subantarctic South Atlantic. Paleoceanography, 17, 1–11.

Billups, K., Pälike, H., Channell, J. E. T., Zachos, J. C., & Shackleton, N. J. (2004). Astronomic calibration of the late Oligocene through early Miocene geomagnetic polarity time scale. Earth and Planetary Science Letters, 224, 33–44. doi:10.1016/j.epsl.2004.05.004

de Boer, A. M., Sigman, D. M., Toggweiler, J. R., & Russell, J. L. (2007). Effect of global ocean temperature change on deep ocean ventilation. Paleoceanography, 22, PA2210.

Brady, H.B. (1884) Report on the foraminifera dredged by H.M.S. Challenger during the years 1873-1876. Report of the scientific results of the voyage of H.M.S. Challenger, 1873-1876, Zoology, 9: 1-814.

Bruch, A.A., Uhl, D., Mosbrugger, V. (2007). Miocene climate in Europe; patterns and evolution; a first synthesis of NECLIME. Palaeogeogr. Palaeoclim. Palaeoec. 253, 1–7.

Clemens, S.C., Prell, W.L., 1991. One-million year record of summer-monsoon winds and continental aridity from the Owen Ridge (Site 722B), northwest Arabian Sea. Ocean Drill. Prog. Sci. Res. 117, 365^388.

Diester-Haass, L., Billups, K., Jacquemin, I., Emeis, K. C., Lefebvre, V., and François, L. (2013) Paleoproductivity during the middle Miocene carbon isotope events: A data- model approach, Paleoceanography, 28, 334-346

Diester-Haass, L., Billups, K., & Emeis, K. (2011). Enhanced paleoproductivity across the Oligocene/Miocene boundary as evidenced by benthic foraminiferal accumulation rates. Palaeogeography, Palaeoclimatology, Palaeoecology, 302, 464–473.

Epstein, S., Buchsbaum, R., Lowenstam, H. & H.C, U. (1953) Revised carbonate-water isotopic temperature scale.. Geological Society of America Bulletin vol. 64, pp. 1315-1325.

Flower, Benjamin P, & Kennett, J. P. (1993). Relations between Monterey Formation deposition and middle Miocene global cooling: Naples Beach section, California. Geology, 21, 877- 880

Flower, B.P., & Kennett, J. P. (1994). The middle Miocene climatic transition: East Antarctic ice sheet development, deep ocean circulation and global carbon cycling. Paleobiology, Paleoclimatology, Paleoecology, 108, 537-555.

Fontugne, M. R., and Duplessy, J. C , 1986. Variations of the monsoon regime during the Upper Quaternary: evidence from carbon isotopic record of organic matter in the North Indian Ocean sediment cores. Palaeogeogr. Palaeoclimatol. Palaeoecol., 56:69

Foster, G.L., Pogge von Strandmann, P.A.E., Rae, J.W.B. (2010) Boron and magnesium isotopic composition of seawater. Geochem. Geophys. Geosyst. 11, Q08015 doi:08010.01029/02010GC003201

Foster, G.L., Lear, C.H., & Rea, J.W.B. (2012). The evolution of pCO$_2$, ice volume and climate during the middle Miocene. Earth and Planetary Science Letters, 341-344, 243-254.

Hodell, D. A. and Woodruff (1994), F.: Variations in the strontium isotopic ratio of seawater during the Miocene: stratigraphic and geochem- ical implications, Paleoceanography, 9, 405–426.

Holbourn, Ann EL; Kuhnt, Wolfgang; Simo, JA; Li, Qianyu (2004): Middle Miocene isotope stratigraphy and paleoceanographic evolution of the northwest and southwest Australian margins (Wombat Plateau and Great Australian Bight). Palaeogeography, Palaeoclimatology, Palaeoecology, 208(1-2), 1-22,

Holbourn, A., Kuhnt, W., Schulz, M., Flores, J.-A., & Andersen, N. (2007). Orbitally-paced climate evolution during the middle Miocene "Monterey" carbon-isotope excursion. Earth and Planetary Science Letters, 261, 534–550. doi:10.1016/j.epsl.2007.07.026

Holbourn, A., W. Kuhnt, M.Lyle, L. Schneider, O. Romero, N. Andersen (2014) Middle Miocene climate cooling linked to intensification of eastern equatorial Pacific upwelling, Geology 42; 19-22 doi: 10.1130/G34890.1

Kennett, J.P (1986): Miocene to early Pliocene oxygen and carbon isotope stratigraphy in the Southwest Pacific, Deep Sea Drilling Project Leg 90. In: Kennett, J.P.; von der Borch, C.C.; et al. (eds.), Initial Reports of the Deep Sea Drilling Project, Washington (U.S. Govt. Printing Office), 90, 1383-1411,

Kürschner, W. M., & Kvaček, Z. (2009). Oligocene- Miocene CO2 fluctuations, climatic and palaeofloristic trends inferred from fossil plant assemblages in central Europe. Bulletin of Geosciences, 84,189–202. doi:10.3140/bull.geosci.1091.

Laskar, J., Robutel, P., Joutel, F., Gastineau, M., Correia, A. C. M., & Levrard, B. (2004). Long-term numerical solution for the insolation quantities of the Earth. Astronomy & Astrophysics, 285, 261–285.

Lear, Caroline H; Mawbey, Elaine M; Rosenthal, Yair (2010). Cenozoic benthic foraminiferal Mg/Ca and Li/Ca records: Toward unlocking temperatures and saturation states Paleoceanography 25, Issue 4 DOI: 10.1029/2009PA001880

Liebrand, D., Lourens, L. J., Hodell, D. A., De Boer, B., Van de Wal, R. S. W., & Pälike, H. (2011). Antarctic ice sheet and oceanographic response to eccentricity forcing during the early Miocene. Climate of the Past, 7, 869–880. doi:10.5194/cp-7- 869-2011

Lourens, L. J. and Hilgen, F. J. (1997) Long-periodic variations in the Earth's obliquity and their relation to third-order eustatic cycles and late Neogene glaciations, Quatern. Int., 40, 43–52.

Miller, K. G., Wright, J. D., & Fairbanks, G. (1991). Unlocking the Ice House: Oligocene-Miocene Oxygen Isotopes, Eustasy, and Margin Erosion. Journal of geophysical research, 96, 6829–6848.

Moore, T.C., Jr., P.D. Rabinowitz, P.E. Borella, N.J. Shackleton, and A. Boersma (1984), DSDP Volume LXXIV, 31. History of the Walvis Ridge doi:10.2973/dsdp.proc.74.131.1984

van Morkhoven, F. P. C. M., Berggren, W. A.,and Edwards, A. S. (1986) Cenozoic cosmopolitan deep-water benthic foraminifera. Bulletin des Centres Recherches Exploration-Production Elf-Aquitaine, Memoir, 11: 1-423.

Mosbrugger, V., Utescher, T., & Dilcher, D. L. (2005). Cenozoic continental climatic evolution of Central Europe. PNAS, 102, 14964–14969. doi:10.1073/pnas.0505267102

O'Leary, M.H. (1988) Carbon isotopes in photosynthesis, Bioscience, 328-336

Pagani, M., Arthur, M. A., & Freeman, K. H. (1999). Miocene evolution of atmospheric carbon dioxide. Paleoceanography, 14, 273–292.

Pälike, H., Norris, R. D., Herrle, J. O., Wilson, P. A, Coxall, H. K., Lear, C. H., Shackleton, N. J., Tripati, A.K., & Wade, B.S. (2006b). The heartbeat of the Oligocene climate system. Science, 314, 1894–1898. doi:10.1126/science.1133822

Pearson, P. N., & Palmer, M. R. (2000). Atmospheric carbon dioxide concentrations over the past 60 million years. Nature, 406, 695–9. doi:10.1038/35021000

Pearson, P. N., & Palmer, M. R. (2000). Atmospheric carbon dioxide concentrations over the past 60 million years. Nature, 406, 695–9.

Pekar, S. F., & DeConto, R. M. (2006). High-resolution ice-volume estimates for the early Miocene: Evidence for a dynamic ice sheet in Antarctica. Palaeogeography, Palaeoclimatology, Palaeoecology, 231(1-2), 101–109. doi:10.1016/j.palaeo.2005.07.027

Pierre, C., Vergnaud-Grazzini, C., Faugeres, J.C. (1991) Oxygen and carbon stable isotope tracers of the water masses in the Central Brasil Basin. Deep-Sea Research 38 (5), 597}606.

Pierre, C. (1999) The oxygen and carbon isotope distribution in the Mediterranean water masses.. Marine Geology vol. 153, p. 41–55.

Paillard, D., Labeyrie, L., & Yiou, P. (1996). Macintosh program performs time-series analysis. Eos Trans, AGU, 77, 379.

Prell, W. L., Kutzbach, J. E. (1987) Monsoon variability over the past 150,000 years. J. Geophys. Res., 92:8411-8425.

Retallack, G.J. (2001) Soils of the Past. Blackwell, Oxford.

Retallack, G. J. (2009) Refining a pedogenic-carbonate CO2 paleobarometer to quantify a middle Miocene greenhouse spike, Palaeogeogr., Palaeoclimatol., Palaeoecol., 281, 57–65, 491, 498, 508

Shackleton, N. J. (1974). Attainment of isotope equilibrium between ocean water and the benthonic foraminifera genus uivergerina: isotopic changes in the ocean during the last glacial. Colloq. Int. Ctr. National Rech. Sci., 219, 203–209.

Sirocko, E, and Sarnthein, M. (1989) Wind-borne deposits in the north- west Indian Ocean: record of Holocene sediments versus modern satellite data. In Leinen, M., and Sarnthein, M. (Eds.), Paleoclima- tology and Paleometeorology: Modern and Past Patterns of Global Atmospheric Transport. NATO ASI Ser., 401-433

Steens, T., D. Kroon, W.G. ten Kate, A Sprenger "18. Late Pleistocene periodicities of oxygen isotope ratios, calcium carbonate contents and magnetic susceptibilies of western Arabian Sea margin Hole 728A" in: Prell, W. L., Niitsuma, N., et al., (1991) Proceedings of the Ocean Drilling Program, Scientific Results, Vol. 117

Thompson, R. & Oldfield, F. (1986) Environmental magnetism, xii+227 pp. (Allen & Unwin, London).

Vincent, E., & Berger, W.H., 1985. Carbon dioxide and polar cooling in the Miocene: the Monterey hypothesis. In: Sundquist, E.T.,

Broecker, W.S. (Eds.), The carbon cycle and atmospheric CO2: natural variations Archean to present, AGU, Washington, DC, 455–468.

Von der Heydt, A. and Dijkstra, H. A. (2008) The effect of ocean gateways on ocean circulation patterns in the Cenozoic, Global Planet. Change, 62, 132–146, 2008. 491, 509

Wade, B. S. and Pälike, H. (2004) Oligocene climate dynamics, Paleoceanography, 19, PA4019, doi:10.1029/2004PA001042.

Warner G. ten Kate, and Antoinette Sprenger (1991) "Late Pleistocene periodicities of oxygen isotope ratios, calcium carbonate contents and magnetic susceptibilities of Western Arabian Sea margin Hole 728A" in: Prell, W. L., Niitsuma, N., et al. (1991) Proceedings of the Ocean Drilling Program, Scientific Results, Vol. 117

Weltje, G.J., R. Tjallingii (2008) Calibration of XRF core scanners for quantitative geochemical logging of sediment cores: Theory and application Earth and Planetary Science Letters 274, 423–438

Woodruff, F., Savin, S. (1991) Mid-Miocene isotope stratigraphy in the deep sea: high resolution correlations, paleoclimatic cycles, and sediment preservation. Paleoceanography 6, 755–806.

Wright, J.D., Miller, K.G., & Fairbanks, R.G. (1992). Early and middle Miocene stable isotopes: implications for deepwater circulation and climate. Paleoceonography, 7, 357–389.

Wright, J.D., & Miller, K.G. (1993). Southern ocean influences on late Eocene to Miocene deepwater circulation. Antarctic research series, 60, 1-25.

You, Y., Huber, M., Müller, R. D., Poulsen, C. J., & Ribbe, J. (2009). Simulation of the Middle Miocene Climate Optimum. Geophysical Research Letters, 36, L04702. doi:10.1029/2008GL036571.

Zachos, J., Pagani, M., Sloan, L., Thomas, E., & Billups, K. (2001b). Trends, Global Rhythms, Aberrations to in global climate to present, Science, 292, 686–693.

Zachos, J. C., Kroon, D., & Blum, P. (2004). Shipboard Scientific Party: Proc. ODP, Init. Repts., 208, Ocean Drilling Program, College Station, TX doi:10.2973/odp.proc.ir.208.2004.